

Understanding beta-lactam-induced lysis at the single-cell level

Felix Wong^{1,2,3,†,*}, Sean Wilson^{4,5,†}, Ralf Helbig⁶, Smitha Hegde⁷, Olga Aftenieva⁶, Hai Zheng⁸, Chenli Liu⁸, Teuta Pilizota⁷, Ethan C. Garner^{4,5}, Ariel Amir^{3,*}, and Lars D. Renner^{6,*}

Correspondence*: Corresponding Authors

fwong@broadinstitute.org,arielamir@seas.harvard.edu,renner@ipfdd.de

2 ABSTRACT

- 3 Mechanical rupture, or lysis, of the cytoplasmic membrane is a common cell death pathway in
- 4 bacteria occurring in response to β-lactam antibiotics. A better understanding of the cellular design
- 5 principles governing the susceptibility and response of individual cells to lysis could indicate
- 6 methods of potentiating β -lactam antibiotics and clarify relevant aspects of cellular physiology.
- 7 Here, we take a single-cell approach to bacterial cell lysis to examine three cellular features—
- 7 Tiere, we take a single deli approach to basterial deli 1933 to examine tirree cellular leatures
- 8 turgor pressure, mechanosensitive channels, and cell shape changes—that are expected to
- 9 modulate lysis. We develop a mechanical model of bacterial cell lysis and experimentally analyze
- the dynamics of lysis in hundreds of single Escherichia coli cells. We find that turgor pressure
- is the only factor, of these three cellular features, which robustly modulates lysis. We show that
- 12 mechanosensitive channels do not modulate lysis due to insufficiently fast solute outflow, and
- that cell shape changes result in more severe cellular lesions but do not influence the dynamics
- of lysis. These results inform a single-cell view of bacterial cell lysis and underscore approaches
- of combatting antibiotic tolerance to β -lactams aimed at targeting cellular turgor.

¹Institute for Medical Engineering & Science, Department of Biological Engineering, Massachusetts Institute of Technology, Cambridge, MA 02142, USA

² Infectious Disease and Microbiome Program, Broad Institute of MIT and Harvard, Cambridge, MA 02142, USA

³John A. Paulson School of Engineering and Applied Sciences, Harvard University, Cambridge, MA 02138, USA

⁴Department of Molecular and Cellular Biology, Harvard University, Cambridge, MA 02138, USA

⁵Center for Systems Biology, Harvard University, Cambridge, MA 02138, USA

⁶Leibniz Institute of Polymer Research and the Max Bergmann Center of Biomaterials, 01069 Dresden, Germany

⁷Centre for Synthetic and Systems Biology, Institute of Cell Biology, School of Biological Sciences, University of Edinburgh, Edinburgh EH9 3FF, United Kingdom ⁸CAS Key Laboratory for Quantitative Engineering Biology, Shenzhen Institute of Synthetic Biology, Shenzhen Institutes of Advanced Technology, Chinese Academy of Sciences, Shenzhen 518055, People's Republic of China

[†]These authors contributed equally to this work.

16 Keywords: antibiotics, cell wall, cell mechanics, turgor pressure, mechanosensitive channels, MreB

1 INTRODUCTION

Understanding how antibiotics work and how to counter antibiotic resistance are two of the most pressing questions in microbiology today. While new antibacterial therapies are still being discovered, the threat of 18 multidrug resistance persists, and more than 35,000 people die of infections caused by antibiotic-resistant 19 microbes each year in the U.S. alone (Centers for Disease Control and Prevention, 2019). Our modern 20 arsenal of antibiotics has largely resulted from screens for inhibitors of bacterial growth in the 1960s 21 22 (Walsh, 2003; Lewis, 2010), and comparatively few antibiotics have since been introduced (Walsh, 2003). Without the discovery of novel antibiotics, it is important to better understand how known bactericidal antibiotics kill bacteria, which could better inform methods of potentiating their lethality. In contrast to 24 studies of antibiotic lethality that have centered on bulk culture measurements (Blair et al., 2015; Kohanski 25 et al., 2010), here we take a single-cell approach to understanding the physical processes underlying cell 26 death by β -lactam antibiotics, the most widely-used class of antibiotics (Bush and Bradford, 2016). 27

In many bacteria, the peptidoglycan (PG) cell wall confers cell shape and sustains the structural integrity 28 of the cell. The structure of this cell wall is a partially-ordered mesh of mechanically stiff glycan strands 29 crosslinked by peptide bonds (Höltje, 1998; Cabeen and Jacobs-Wagner, 2005; Turner et al., 2013). In 30 Gram-negative bacteria such as Escherichia coli, the thin cell wall is sandwiched between the inner and 31 outer membranes, while in Gram-positive bacteria the thicker cell wall encloses a single cytoplasmic 32 membrane. In both Gram-negative and Gram-positive bacteria, the cell wall and membranes collectively 33 comprise the cellular envelope. The cell envelope resists the internal turgor pressure, an outward normal 34 force exerted on the cell envelope by the cytoplasm, and, in bacteria including E. coli, the cell wall is 35 maintained by penicillin-binding proteins (PBPs) and conserved membrane proteins (Cabeen and Jacobs-36 Wagner, 2005; Jones et al., 2001; Paradis-Bleau et al., 2010; Typas et al., 2012; Meeske et al., 2016; Cho 37 et al., 2016). β -lactams inhibit PBP activity and the formation of peptide crosslinks (Qiao et al., 2017; Cho 38 et al., 2014; Falconer et al., 2011). PBP inhibition is believed to result in the formation of holes in the cell 39 wall which destabilize the cytoplasmic membrane and drive subsequent lysis (Chung et al., 2009; Huang 40 et al., 2008; Yao et al., 2012; Wong and Amir, 2019; Cushnie et al., 2016). 41

There are numerous cellular features that may influence β -lactam-induced lysis at the single-cell level. 42 While previous studies have assumed that turgor pressure drives cellular lysis (Yao et al., 2012; Wong and 43 Amir, 2019; Reuter et al., 2013), the turgor pressure could be regulated by cellular processes including the 44 gating of mechanosensitive channels (MSCs) (Reuter et al., 2013; Bialecka-Fornal et al., 2015; Levina 45 et al., 1999; Haswell et al., 2011; Chure et al., 2018), which occurs as fast as milliseconds (Boer et al., 2011; 46 Çetiner et al., 2017). Studies of the response of cells to hypoosmotic shocks, in which the osmolarity of the 47 environment is suddenly decreased, have indicated a typical timescale for cellular volume recovery of ~ 1 48 min (Buda et al., 2016), comparable to the timescales of β -lactam-induced lysis (Yao et al., 2012; Wong and 49 Amir, 2019). Additionally, as β -lactams inhibit peptidoglycan cell wall synthesis, the shape of a bacterium, 50 as determined by its cell wall, may also influence—and be influenced by— β -lactam treatment. Indeed, 51 numerical simulations have suggested that the response of E. coli cell shape to vancomycin treatment 52 in susceptible cells reveals information on cell wall architecture (Huang et al., 2008). Building on these 53 studies, here we sought to better understand the effects of three cellular features—turgor pressure, MSCs, 54 and cell shape changes—on β -lactam-induced lysis. In addition to informing a single-cell view of bacterial 55 cell lysis, our findings clarify the physiological features influencing the response of bacterial cells to 56 β -lactam antibiotics. 57

2 RESULTS

58

78

79

80

81

82

83

84

85

86

87

2.1 Mechanics of bacterial cell lysis

59 Recent studies have characterized the dynamics of lysis in E. coli cells treated with β -lactams (Wong and Amir, 2019; Yao et al., 2012; Zahir et al., 2020, 2019). In previous work, Yao et al. studied the 60 61 dynamics of lysis in single cells treated with cephalexin and ampicillin using high-resolution microscopy 62 (Yao et al., 2012); here, we build on this study to explore additional perturbations involving turgor pressure, mechanosensitive channels (MSCs), and cell shape changes. Antibiotic-treated E. coli cells 63 64 exhibit distinctive morphological features at the single-cell level, in contrast to bulk culture, in which 65 cell death is primarily reflected by decreases in optical density (Figures 1A and S1). When treated with cephalexin, a β -lactam which inhibits cell division by blocking the activity of various PBPs including PBP3, 66 67 a division-specific PBP (Falconer et al., 2011; Chung et al., 2009; Kocaoglu and Carlson, 2015; Curtis et al., 68 1979), cells become filamentous and typically exhibit two distinct phases. Bulging, the development of an initial membrane protrusion after ~ 1 h of cephalexin treatment, occurs on a timescale of seconds. Swelling, 69 70 the growth of the protrusion, occurs on a timescale of minutes and is followed by explosive lysis (Figure 71 1B-D). These phenotypes also arise under ampicillin treatment (Figure S1), underscoring the generality 72 across different β -lactams. We first sought to further develop a physical model of membrane bulging and 73 swelling (Wong and Amir, 2019) to predict the influence of turgor pressure, MCSs, and cell shape changes 74 on lysis dynamics. The model relies on the mechanical properties of the cell envelope and coarse-grains more detailed sources of variation in the cell envelope, including lipid and peptidoglycan composition. 75 76 Thus, while we detail our model for a Gram-negative bacterium here, the model can be extended to the 77 case of a Gram-positive bacterium which has only one cell membrane, as discussed further in *Methods*.

We model the cell wall, inner membrane, and outer membrane of an *E. coli* cell as thin, homogeneous, elastic layers, with the inner membrane enclosing a large number of solutes which collectively and entropically generate a turgor pressure on the order of 1 atm (Deng et al., 2011; Koch, 1983; Cayley et al., 2000). Unlike the rigid cell wall, both membranes are viewed as fluid, and membrane phospholipids are assumed to rearrange around membrane-cell wall anchors. The assumption of membrane fluidity implies that the mechanical stresses in the membranes are spatially homogeneous and isotropic. The free energy of the cellular envelope and the volume it encloses comprise elastic stretching and bending terms, in addition to a pressure-volume work due to the turgor pressure (Wong and Amir, 2019). The equilibrium state of a cell, describing both the cell shape and the mechanical stresses imparted by turgor pressure inside the cellular envelope, can be found by minimizing the free energy (*Methods*).

88 Upon introducing a hole in the cell wall, minimizing the free energy predicts the formation of a partially-89 subtended, spherical membrane bulge; we solve the model to obtain detailed predictions in the *Methods* 90 (Figures S2-S4). Importantly, the model predicts that the bulge is in equilibrium, so that the bulge stresses 91 are pR/2, where p is the turgor pressure and R is the bulge radius. The model also predicts that, in the 92 cylindrical body of the cell, the mechanical stresses in all cell envelope components sum to pw/4 and pw/2in the axial and circumferential directions, respectively, where w is the rod width: here, the membranes 93 can be load-bearing in addition to the cell wall, a prediction consistent with recent experimental and 95 modeling studies (Rojas et al., 2018; Shaevitz, 2018; Hwang et al., 2018; Wong and Amir, 2019). For lysis to occur, the model requires that the cell membranes are sufficiently stressed. Thus, the model predicts that 96 97 decreasing cellular turgor contributes to decreased mechanical stresses in the bulge and increased bulge 98 stability. We sought to test this prediction and explore the effects of related features, including MSCs and cell shape changes, as discussed further below, experimentally (Figure 1F). 99

2.2 Osmotic stabilization delays, but does not prevent, lysis

100

141

101 Previous studies have assumed that the lysis of bulged cells is driven by turgor pressure (Yao et al., 2012; 102 Wong and Amir, 2019; Reuter et al., 2013), as predicted here by our model. Indeed, recent studies have shown that the osmotic stabilization of cell cultures contributes to β -lactam tolerance (Thulin et al., 2017; 103 Mickiewicz et al., 2019). However, at the single-cell level, the turgor pressure could be regulated by MSCs 104 and other processes on timescales comparable to, or less than, the timescales of bulging and swelling 105 (Reuter et al., 2013; Boer et al., 2011; Cetiner et al., 2017; Bialecka-Fornal et al., 2015; Buda et al., 2016). 106 To examine turgor pressure as a driver of lysis in single cells, we quantified two statistics—the bulge 107 lifetime and the yield bulge radius—in our experiments lysing log-phase, wild-type cells with cephalexin 108 treatment at a concentration of 50 μ g/mL, corresponding to $\sim 2.5 \times$ the minimum inhibitory concentration 109 (MIC; Table S1 and Figure 1B-D). Here, a cell's bulge lifetime is the time between bulging and lysis given 110 that the cell eventually lyses, and a cell's yield bulge radius indicates the final size of the bulge (Figure 1D). 111 We next stabilized populations of bulged cells with flow of hyperosmotic media in microfluidic chambers 112 113 (Figure 2A and Movie S3).

114 In these experiments, growth media with the same concentration of cephalexin and varying concentrations of sorbitol, a sugar alcohol used in previous studies of osmotic shocks (Rojas et al., 2014), were introduced 115 to populations of cells by flow at the onset of bulging (see *Methods* for details). As a control, untreated 116 cells were similarly shocked by flow of medium containing 500 mM sorbitol: such cells shrank in length 117 by \sim 7%, recovered, and did not lyse, consistent with previous investigations of hyperosmotic shocks in E. 118 119 coli (Figure S5) (Pilizota and Shaevitz, 2012). Hyperosmotically shocking cephalexin-treated cells, we found that the lifetimes of both existing and newly-forming bulges were longer for large enough sorbitol 120 concentrations, including those (\sim 50 mM) corresponding to estimated values (\sim 1 atm) of E. coli's turgor 121 pressure (Figure 2B and 2D) (Deng et al., 2011; Koch, 1983; Cayley et al., 2000). In particular, cells under 122 hyperosmotic shock typically persisted for tens of minutes after bulging—a timescale comparable to the 123 half-life of cephalexin in humans (Gower and Dash, 1969)—in contrast to ~3 minutes for non-osmotically 124 shocked cells (Figure 2D). Furthermore, we observed a statistically significant increase in bulge lifetime 125 even with flow of 0 mM sorbitol, an effect which arises because bulges can be detached from cells by the 126 flow and remain stable without further growth, as observed empirically (Figure S5). Although the fractions 127 of bulged cells remained similar across all conditions involving osmotic shocks (Figure S6), the addition 128 of hyperosmotic media and ensuing longer bulge lifetimes of osmotically-shocked cells correlate with 129 increased survival rates of single cells (Figure S1). Thus, these findings are consistent with the hypothesis 130 that turgor pressure is crucial to lysis. Consequently, they support modulation of cellular turgor as a process 131 that can result in β -lactam tolerance. This process does not depend on changes to the MIC (Table S1); 132 rather, it depends on the phenotypic response of cells. 133

While flow of hyperosmotic media could delay lysis, we also observed that cells ultimately lysed. For long enough times, this lysis occured irrespective of the external osmolarity and therefore is not likely to arise from biased sampling (Figure S6). Furthermore, measurements showing similar bulge radii at lysis (Figure 2C and 2E) suggest that lysis may occur due to recovery of cellular turgor, as the model predicts that the bulge stresses $\sigma = p(t)R(t)/2$ must increase for lysis to occur. Thus, consistent with the minute-timescale recovery of cellular turgor in response to hyperosmotic shock (Pilizota and Shaevitz, 2014), regulatory processes appear to restore the turgor pressure and eventually cause lysis.

2.3 Mechanosensitive channels fail to protect against lysis

As turgor pressure appears to be re-established for lysis in osmotically shocked cells, we asked whether physiological mechanisms such as osmoregulation through MSCs could affect lysis dynamics. It has been

shown that MSCs are crucial for preventing lysis in various environments, such as those involving osmotic 145 downshifts and variations in membrane tension (Reuter et al., 2013; Bialecka-Fornal et al., 2015; Levina et al., 1999; Haswell et al., 2011; Chure et al., 2018), and prior studies have suggested that MSCs gate 146 147 as fast as milliseconds (Boer et al., 2011; Cetiner et al., 2017). Experiments examining the response of 148 MSCs to hypoosmotic shocks reveal a typical timescale for cellular volume recovery of ~ 1 min (Buda et al., 2016). Consistent with this study, after application of a 600 mM hypoosmotic shock, we observed 149 150 both volume recovery on a timescale of ~ 30 s and a characteristic overshooting (Buda et al., 2016) on a 151 timescale comparable to 1 min in wild-type cells (Figures 3A and S7). Additionally, quantitative estimates 152 of membrane tension suggest that its increase (\sim 11 mN/m) is sufficient to trigger MSCs in many bulged 153 cells, as typical gating tensions are 5 to 15 mN/m (Buda et al., 2016)—a range less than, or comparable 154 to, typical estimated lytic tensions of 10 to 20 mN/m, corresponding to membrane yield strains of $\sim 10\%$ (Wong and Amir, 2019; Chabanon et al., 2017; Li et al., 2013) and membrane area stretch moduli of 0.1 to 155 156 0.2 N/m (Sun et al., 2014) (see *Methods* for additional details). Such a response could therefore contribute 157 to bulge stability and underlie a role of MSCs in resisting the lysis we observed. However, the role of MSCs in β -lactam-mediated lysis does not seem to have been studied previously. 158

159 To probe the effects of individual MSCs on lysis, we lysed genetic knockouts of the MSC of small 160 conductance (MscS), the MSC of large conductance (MscL), and an aquaporin (AqpZ) from the Keio 161 collection of single knockout strains (Baba et al., 2006). As we found that the cephalexin MICs for all 162 strains are similar to that of wild-type cells (Table S1), we used an identical concentration of 50 μ g/mL 163 as above. We observed that the lysis dynamics of all strains were largely similar to that of wild-type. We 164 found statistically significant differences in the yield bulge radii of the $\triangle aqpZ$ strain, and cannot rule out 165 the possibility that AqpZ may influence the dynamics of β -lactam-induced lysis. Nevertheless, the average 166 bulge lifetimes and sizes are within a two-fold range in all single knockouts (Figures 3B, 3C, and S7), 167 suggesting that these individual MSCs do not substantially protect against lysis.

We next asked whether, instead of any single MSC, the collective action of several MSCs elicited a 168 stronger response, as is the case when cells are hypoosmotically shocked (Buda et al., 2016). To address 169 this question, we interrogated the recently constructed " $\Delta 2$ " and " $\Delta 7$ " strains of E. coli in which two ($\Delta 2$) 170 171 and all (Δ 7) the major MSCs are genetically deleted (Buda et al., 2016; Hegde, 2020). The deleted channels 172 comprise MscS and MscL (Δ 2), the MSC of miniconductance (MscM), the potassium-dependent MSC (MscK), and three MscS homologs (YnaI, YbiO, and YbdG) (Edwards et al., 2012). We validated that the 173 channels function in wild-type cells by examining traces of volume recovery in response to hypoosmotic 174 175 shocks (Figures 3A and S7). Intriguingly, we found that the lysis dynamics of both the $\Delta 2$ and $\Delta 7$ strains were quantitatively similar to that of wild-type (Figures 3B, 3C, and S7 and Movie S5). As with the single 176 knockouts, $\Delta 2$ and $\Delta 7$ cells exhibited bulge lifetimes and sizes approximately equal to those of wild-type 177 178 cells (Figure 3B and 3C), and, as explained above, our model suggests that the similar bulge sizes at lysis imply that these cells have similar turgor pressures. Thus, while studies have shown the importance of 179 MSCs in relieving membrane tension and responding to osmotic shifts (Reuter et al., 2013; Bialecka-Fornal 180 et al., 2015; Levina et al., 1999; Haswell et al., 2011; Chure et al., 2018), our observations suggest that 181 182 MSCs fail to protect against membrane bulging and lysis.

To better understand the apparent failure of MSCs to protect against lysis, we extended our model of bacterial cell lysis to account for the gating of MSCs and the transport of solutes. As detailed in the *Methods*, 184 we assume MSC gating to be well described by the addition of nanoscale gaps in the inner membrane (Buda et al., 2016; Naismith and Booth, 2012). We modeled the laminar outflow of intracellular solutes to the external milieu and calculated the mechanical stresses in a bulged cell as a function of time after MSC

183

185 186

187

gating (Figures S3 and S4). Consistent with our experimental observations, the model predicts that the decrease in turgor elicited by MSC gating is insufficient to overcome the increase in membrane stresses due to bulge growth (Figure S4). Namely, while solute outflow through MSCs substantially decreases the membrane tension in an unbulged cell, in a bulged cell the membrane bulge is unsupported by the cell wall and growing in time. The bulge stresses of $\sigma = p(t)R(t)/2$ are therefore carried by the membranes and increase in time due to the dependence on R(t). We find that this increase counteracts the decreases in membrane tension arising from solute outflow through MSCs (Figure S4). Thus, the combination of our experimental observations and our biophysical model of solute transport indicate that MSCs, even when gated, can be insufficient to resist lysis.

2.4 Altering E. coli cell width changes cell shape, but not susceptibility to lysis

Finally, we sought to use our model to predict whether cell shape changes may affect lysis. As detailed in the *Methods*, our model predicts wider cells to yield larger bulges due to the energetic trade-offs between mechanical stresses in the cylindrical bulk of the cell and stresses in the bulge (see *Methods* for details). We therefore sought to experimentally test this prediction by generating *E. coli* cells of different widths.

To modulate cell width, we used an *mreB*-titratable strain of *E. coli* we previously constructed (Zheng et al., 2016). MreB is an actin homolog crucial to the cell wall synthesis required for rod shape (Jones et al., 2001; Garner et al., 2011; Domínguez-Escobar et al., 2011; van Teeffelen et al., 2011; Hussain et al., 2018; Wong et al., 2019) whose inhibition by a small molecule, A22, results in cell wall weakening and eventual lysis under typical growth conditions (Wang et al., 2010; Furchtgott et al., 2011; Tuson et al., 2012; Gitai et al., 2005; Bean et al., 2009). In the *mreB*-titratable strain, the expression of *mreB* is controlled by an inducer, anhydrotetracycline (aTc), of a P_{tet} -tetR feedback loop, while the native copy of *mreB* was removed. Above a threshold concentration of 1 ng/mL aTc, decreasing aTc concentration increases cell width (Figure 4A) while leaving the growth rate unchanged, as previously described (Zheng et al., 2016).

In the mreB-titratable strain, we found that the cephalexin MIC was similar to that of wild-type cells (Table S1), and hence, we induced lysis as above with cephalexin at the same concentration of 50 μ g/mL. We observed that cells treated with cephalexin lost shape before membrane bulging (Figure 4B and C). These "lemon-shaped" cells exhibited varying widths along the cellular long axis over a range of aTc concentrations, with larger widths and greater heterogeneity at smaller concentrations of aTc. Regions of large widths, apparently positioned at septa, were commonly flanked by narrower cross-sections and resemble Bacillus subtilis cells with perturbed PG precursor pathways (Peters et al., 2016; Zhao et al., 2016). Intriguingly, and in contrast to wild-type cells, growth became isotropic in cells with severe width heterogeneity (Figure 4D), an observation which could result from misinsertion of glycan strands during PG synthesis (Hussain et al., 2018) and severely disordered wall architecture (Dion et al., 2019).

Quantifying the lysis dynamics of *mreB*-titratable cells, we found that these cells lysed similarly to wild-type cells, with membrane bulging and lysis occurring on characteristic timescales of seconds and minutes, respectively, approximately 1 h after antibiotic treatment (Figures 4E and S8, and Movie S6). Consistent with model predictions, decreasing aTc concentration correlated with larger cell widths and increased bulge radii (Figure 4F). Yet, we found that cells with larger bulges did not lyse sooner (Figure S8), as would be expected from our model if the turgor pressure were similar across cells of different cell widths. Measurements of the bulge radii at lysis of *mreB*-titratable cells in 3 ng/mL aTc further revealed that yield bulge radii were, on average, twice as large as that of wild-type cells (Figure 4F). As we expect that the membrane composition, and hence membrane yield strain, are similar across cells, this observation suggests that the turgor pressure of *mreB*-titratable cells in the presence of 3 ng/mL aTc is, on average, half the turgor pressure of wild-type cells at lysis (Figure 4F). Intriguingly, this observation suggests that, in

unbulged mreB-titratable cells, the mechanical stresses (proportional to pw) in the cell envelope remain approximately constant across different cell widths, w (Figure 4G).

In sum, these results reveal the effect of cell shape changes on lysis and offer biological insight into cell width maintenance. Our observations suggest that cell width changes in growing *mreB*-titratable cells may not be explained by differences in turgor pressure alone: *mreB*-titratable cells do not increase their widths by increasing turgor pressure and thus cell wall strain, as our measurements suggest that the turgor pressure is *decreased* in wider cells. Rather, both turgor pressure and cell wall synthesis may be modulated to generate cells of different widths, and our results provide evidence that the mechanical stresses in the cell envelope are regulated during the normal growth of cells. Indeed, the response of cells to osmotic stress, both hypoosmotic and hyperosmotic, has been appreciated as physiologically relevant in other contexts (Sleator and Hill, 2002), including the conversion of walled cells to wall-less L-forms (Osawa and Erickson, 2019; Chikada et al., 2021; Mickiewicz et al., 2019; Ramijan et al., 2018; Claessen and Errington, 2019). We anticipate future experiments, for instance those involving osmotic shocks, to further validate the hypothesis that the mechanical stresses in cells of different widths are approximately constant.

3 DISCUSSION

234235

236

237238

239

240241

242

243244

245

261

262263

264

265266

267

268

269

270

271

246 Here, we have taken a single-cell approach to quantifying bacterial cell lysis across hundreds of E. coli 247 cells under different physical, genetic, and physiological perturbations. We further developed a biophysical 248 model which explains how lysis emerges as a mechanical response and suggests that the gating of MSCs are insufficient to resist lysis. Experimental results suggest that E. coli cells re-establish their turgor pressure 249 irrespective of lysis and that MSCs, though active, are insufficient to prevent lysis. Furthermore, our 250 251 experiments involving cell shape changes suggest that cells may regulate mechanical stresses in their cell envelopes during normal growth, and that variation in cell width does not affect the dynamics of lysis. 252 253 Taken together, these results suggest that MSCs and MreB do not significantly affect the dynamics of lysis underlying β -lactam killing. In contrast, our work indicates that combination approaches which increase 254 cellular turgor, such as jointly treating cells with hypoosmotic shocks, may be particularly effective in 255 256 countering phenotypic tolerance to β -lactams. As bacterial growth quickly resumes in antibiotic-treated, 257 osmotically-stabilized cultures (Figure S1), our study further indicates that changes in the osmolarity of cellular environments can have clinical implications on the efficacy of β -lactams. While this notion 258 has been appreciated in previous studies (Thulin et al., 2017; Mickiewicz et al., 2019), the present study 259 underscores its single-cell basis. 260

More generally, our study demonstrates how combining theoretical modeling with physical, genetic, and physiological perturbations can reveal insight into the processes governing bacterial cell lysis. This approach to interrogating living cells may be broadly applicable for systems-level analyses of bacterial growth and bacterial stress responses, for which many molecular details remain obscure. We expect future studies to explore other cell death pathways, such as those induced by other antibiotics (Wong et al., 2021), at the single-cell level.

4 METHODS

4.1 Bacterial strains

For the convenience of readers, we have listed the genotypes and sources of all strains used in this study in Table S1. The wild-type strain of E. coli largely used in this study is MG1655, and we verified that the morphological dynamics are statistically indistinguishable in three other wild-type-like strains, JOE309, BW25113, W3110. Strains from the Keio collection of E. coli single knockouts, JW2891-2 ($\Delta mscS$),

Running Title Wong et al.

JW3252-1 ($\triangle mscL$), and JW0859-5 ($\triangle aqpZ$) have previously been described (Baba et al., 2006). These 272 strains were verified by PCR and grown in the presence of 25 μ g/mL kanamycin for selection. The $\Delta 2$ 273 and $\Delta 7$ strains of E. coli have been described in previous work by the Pilizota lab (Buda et al., 2016; 274 Hegde, 2020). These strains were constructed by knocking out up to a total of seven MSCs found in E. coli 275 (Schumann et al., 2010) and grown in the presence of no antibiotics. We verified their genotypes using 276 277 PCR. The *mreB*-titratable strain of *E. coli* has been described in previous work by the Liu lab (Zheng et al., 2016). In this strain, an *amp-P*_{tet}-*tetR-mreB* element was inserted into the chromosomal *attB* site of *E. coli* 278 K12 AMB1655 and the native copy of mreB was replaced by a kanamycin-resistance gene. The strain was 279 cultured in the presence of 50 μ g/mL ampicillin, 25 μ g/mL kanamycin, and 50 ng/mL aTc for plasmid 280 selection.

4.2 **Bacterial culture and growth**

281

282

283 284

285

286

287

288

289

290

291

292

293

294

295

296

297 298

299

300

301

302 303

304

305

306

307

308

309

Cells were grown at 37°C in liquid LB (Bertani, 1951, 2004) (LB: 10 g/L tryptone, 5 g/L yeast extract, 10 g/L NaCl) and, if required, supplemented with appropriate antibiotics. LB media containing 1.5% Difco agar (w/v), supplemented with appropriate antibiotics, was used to grow individual colonies. Tryptone, yeast extract, peptone, Petri dishes, and bacteriological agar were from Becton Dickinson (Sparks, MD) and sodium chloride was from Fisher Scientific (Fairlawn, NJ). Cells were grown from a single colony in LB, supplemented with appropriate antibiotics if required, at 37°C in 14 mL Falcon tubes (Corning, NY) and placed in a roller drum agitating at 60 rpm overnight. The overnight culture was then diluted 1:100 in fresh LB (with aTc at an appropriate concentration for *mreB*-titratable cells), and cells were allowed to grow in the same conditions for approximately 2 h to an optical density (OD₆₀₀) in the range of 0.1 to 0.3, as measured in 2 mL working volumes using a Biowave Cell Density Meter CO8000 (VWR, Radnor, PA). Cells were then concentrated once by centrifugation at 3000 rpm for 5 min, the supernatant was discarded, and cells were resuspended. For experiments involving agarose pads, we placed 1-2 μ L of the concentrated bacterial culture on No. 1.5 coverslips (VWR, Radnor, PA) and immediately placed a 1 mm thick LB agarose (1.5%) pad on top. Cells were imaged directly afterward, so that the total time from taking cells out of culture and start of imaging was \sim 5 min. As we have done before for spheroplast formation (Renner and Weibel, 2011; Renner, 2019) and lysis (Wong and Amir, 2019), we treated cells with the β -lactam antibiotic cephalexin. Cephalexin hydrate (Sigma-Aldrich, St. Louis, MO) was dissolved in 1 M ammonium hydroxide stock solution. Freshly-prepared cephalexin (final concentration 50 μ g/mL) and, when appropriate, aTc (Sigma-Aldrich, St. Louis, MO), were mixed with LB agarose melt before gelation—that is, at a temperature of approximately 55°C—to the final concentrations indicated. Cephalexin (final concentration 50 μ g/mL) and, when appropriate, sorbitol, were added to liquid LB for microfluidic experiments, as detailed below. Note that, for the concentrations of sorbitol considered in this work, the osmolarity of the solution scales linearly with the osmolality (Rojas et al., 2014). Furthermore, while sorbitol can be metabolized by E. coli (Aidelberg et al., 2014), we note here that addition of sorbitol at the concentrations considered serves mainly to increase the total external media concentration, consistent with previous work by others (Rojas et al., 2014).

Microfluidics

For osmotic stablization experiments, we used both custom-made and commercially-available setups. 310 Briefly, we used the commercially-available CellASIC ONIX2 Microfluidic System (Merck, Germany) as 311 follows. Bacteria were grown by diluting an overnight culture 1:200 in fresh LB to an OD₆₀₀ of between 312 0.1 to 0.2 and incubating at 37°C. The bacterial solution was loaded into the appropriate channels using 313 the manufacturer's pre-set loading sequence. After loading, the solution was immediately exchanged to LB+cephalexin (50 μ g/mL) to induce cell lysis. At the onset of bulging, the LB+cephalexin solution was 315 switched to LB+cephalexin+sorbitol to stabilize bulges, and the channels were continuously supplied with

fresh LB+cephalexin+sorbitol at a flow rate of \sim 0.2 μ L/h (corresponding to a set pressure of 0.5 kPa in the CellASIC system). 318

We also used simple, custom-made microfluidic setups comprising rectangular channels with lowered 319

- centers. These devices were designed in AutoCAD (Autodesk, San Rafael, CA), fabricated using in-house 320
- 321 UV lithography, and replicated in polydimethylsiloxane (PDMS) by soft lithography (Weibel et al., 2007),
- 322 as described previously (Renner and Weibel, 2011).

4.4 Microscopy

323

337

347

349

324 We used a Nikon Eclipse Ti inverted microscope (Nikon, Tokyo, Japan) with an enclosing custom-made 325 incubation chamber and equipped with a 6.5 μ m-pixel Hamamatsu ORCA-Flash4.0 V2 sCMOS camera 326 (Hamamatsu, Hamamatsu City, Japan) and a Nikon Plan Apo λ 100x/1.45NA objective (Nikon, Tokyo, 327 Japan) for imaging. We also used a Zeiss Axiovert 200 inverted microscope (Zeiss, Jena, Germany) with an enclosing custom-made incubation chamber and equipped with an Axiocam 503 mono CCD (Zeiss, 328 329 Jena, Germany) and a Zeiss EC Plan-Neofluar 40x/0.75NA objective (Zeiss, Jena, Germany). All cells 330 were imaged at 37°C inside the custom-made incubation chambers. The time between each frame during timelapse measurements ranged from 5 ms to 2 s, and the duration of timelapses varied from 10 min 331 332 to 3 h. Images were recorded using NIS-Elements (Nikon, Tokyo, Japan) and AxioVision (v.4.8, Zeiss, 333 Jena, Germany). We used ImageJ (NIH, Bethesda, MD) for cropping timelapses and the StackReg plugin (Thévenaz et al., 1998), which recursively aligns images in a sequence with geometric transformations, to 334 335 correct for microscope drift as necessary. All microscopy experiments were performed independently on 336 these two different imaging setups and replicated at least twice on each setup.

Bulk culture measurements

We verified similar growth of all strains by measuring growth curves, as shown in Figure S1. Briefly, cells 338 were diluted 1:100 in fresh LB from an overnight culture into 14 mL Falcon tubes and allowed to grow to 339 an OD_{600} of approximately 0.2 in the growth conditions described above, with the appropriate phenotype 340 induced for mreB-titratable cells. Cephalexin (final concentration 50 μ g/mL) was then added, in addition to 341 appropriate concentrations of sorbitol for osmotic shock experiments only. The OD_{600} was measured at 342 various time points. The experiment was independently performed in 96-well plates using a Tecan Genios 343 plate reader (Tecan, Switzerland) and a total volume of 250 μ L per well to confirm the qualitative behaviors 344 of the curves shown in Figure S1. Each experiment was performed at least in biological duplicate. 345

4.6 Image analysis 346

Lysis dynamics were annotated manually in ImageJ (National Institutes of Health, Bethesda, MD). We analyzed a total of 463 wild-type (MG1655, JOE309, BW25113, W3110) cells in control (agarose pad) 348 experiments, 49 wild-type (MG1655) cells in control flow experiments, 77 wild-type (MG1655) cells in flow experiments at a sorbitol concentration of 50 mM, 27 wild-type (MG1655) cells in flow experiments 350 351 at a sorbitol concentration of 250 mM, 80 $\Delta mscS$ cells, 60 $\Delta mscL$ cells, 109 $\Delta aqpZ$ cells, 125 $\Delta 2$ cells, 352 201 Δ 7 cells, 85 mreB-titratable cells at an aTc concentration of 50 ng/mL, and 212 mreB-titratable cells at an aTc concentration of 3 ng/mL. Experiments were not randomized, and we were not blinded to allocation 353 354 during experiments and assessment of results. All cells for which we could resolve bulging and lysis were 355 used.

356 The shapes of individual cells were annotated with subpixel resolution as follows. Bulged cells were 357 fit to cylinders with protruding spheres to determine bulge radii and defect lengths (taken here to be the 358 neck-to-neck lengths of bulges). The bulge lifetime was determined as the time in which a bulge of radius larger than a predetermined threshold value, $0.2 \mu m$, appeared and lysed. In the rare case that cells exhibited 359

Running Title Wong et al.

multiple bulges, we annotated only the bulge which lysed first. To account only for bulging cells, we removed from the data all cells which bulged and lysed within a single timestep of our imaging or 1 s, whichever was larger. We also removed from the data all cells in which the bulge dimensions could not be visually determined, often because the bulge was occluded or moved out of the imaging plane. For each bulge, the bulge radius at lysis was fit in the frame immediately before lysis. The yield defect length was also measured for this frame. For Figure 4F of the main text, the implied turgor pressure was calculated as $p_{\rm IM} = p_{\rm WT} \langle R_{\rm WT} \rangle / R_{mreB}$, where $p_{\rm WT}$ is the turgor pressure of a wild-type (WT) cell, assumed to be constant over cells, $\langle R_{\rm WT} \rangle$ is the yield bulge radius of wild-type cells in control experiments, averaged over the entire population, and R_{mreB} is the yield bulge radius of mreB-titratable cells. The standard deviations in Figure 4G of the main text were calculated assuming all variables to be statistically independent and using the variance relation $Var(XY) = Var(X)Var(Y) + Var(X)\langle Y \rangle^2 + Var(Y)\langle X \rangle^2$, where X and Y are random variables and $\langle \cdot \rangle$ denotes their means (Goodman, 1960).

Cell volume dynamics

360

361

362

363

364

365

366

367

368

369

370

371

372

373 374

375

376 377

378

379 380

381

382

383

384

385

386 387

388

389 390

391

392

393

394

395

401

402

In Figure S7A, E. coli Δ 7 cells with pWR21 were grown in modified M9 (MM9) media, in which the potassium phosphate salts in the regular M9 salts were replaced with sodium phosphate salts (Harbor, 2010), and supplemented with 0.3% glucose, minimal essential amino acids, and an additional 300 mM NaCl. pWR21 contained constitutively expressing cytoplasmic eGFP that was used for cell cytoplasmic volume measurement (Pilizota and Shaevitz, 2012). Cells were cultured at 37°C to an OD₆₀₀ of 0.3–0.5 aerobically with shaking at 220 rpm. Cells were next attached to a microscope tunnel slide using poly-L-lysine as previously described (Buda et al., 2016). Cells were then imaged with an epifluorescence microscope (Nikon CFI Plan Apochromat λ 100x/1.45NA objective, Nikon, Tokyo, Japan) at 21°C, and the field of view was stabilized using back-focal-plane inferometry (Pilizota and Shaevitz, 2012). A 300 mM (460 mOsmol) hypoosmotic shock was delivered by flushing with 35 μ L MM9 media with no additional NaCl, and the tunnel ends were sealed with a liquid sealant (CoverGrip TM Coverslip Sealant, Biotium, Fremont, CA) to avoid drying of the slide. Images were captured every 0.33 s with excitation at 500 nm and emission at 515 nm. Cells uniformly attached to the coverslip were selected for analysis. For Figure 3A, the same protocol was repeated with E. coli BW25113 in LB media—the same media used in all lysis experiments—and 600 mM sorbitol. We note that previously, we observed at the single-cell level that upon downshock, cells expand quickly (several seconds) and continue to recover on a timescale of tens of seconds (Buda et al., 2016). In this previous study, cells were grown in M9 medium as described in the preceding paragraph and supplemented with NaCl to increase the osmolarity. Despite the difference in growth condition and the solute used to increase the osmolarity between ref. (Buda et al., 2016) and Figure 3A, the response we observed to the downshock is similar. This is expected as the downshock is a passive response. Figure S7 shows the $\Delta 7$ strain subjected to a similar downshock magnitude as in Figure 3A and in the same growth condition as in previous work (Buda et al., 2016); for comparison, wild-type traces from previous work (Buda et al., 2016) are included in Figure S7.

The cell volume dynamics during osmotic downshocks were analyzed as previously described (Pilizota 396 and Shaevitz, 2012; Buda et al., 2016). Briefly, cytoplasmic fluorescent protein was used to mark the 397 cell and the total number of pixels whose intensity was above a selected normalized threshold value was 398 399 counted. Individual cell volume traces were normalized by the average volume calculated from the first ten time points. 400

4.8 Statistical testing

The confidence intervals for all bulge parameters in this work were calculated by bootstrapping with 10,000 subsamples using MATLAB's bootci function (Table S3). We note here that we also found that 403

the distributions of bulge radii and and bulge lifetimes could usually be described by the lognormal and 404 exponential distributions, as verified using a χ^2 goodness-of-fit test at a standard $\alpha = 0.01$ significance 405 level; for most conditions, we found that the test result does not reject the null hypothesis that the data come 406 from the corresponding distributions (Table S3). Unless otherwise specified, in order to compare samples 407 from different conditions without assuming specific underlying distributions, two-sample Kolmogorov-408 Smirnov tests were performed for all datasets shown in the main text at the $\alpha = 0.001$ significance level 409 as to reduce the likelihood of Type I (false positive) error. As mreB-titratable cells differ in shape with 410 and without cephalexin, we bootstrapped the cell width statistics (w) of Figure 4A to calculate confidence 411 intervals for Figure 4G of the main text. 412

4.9 MIC determination

413

We determined cephalexin MICs for all strains considered in this work by inoculating a 1:10,000 dilution of an overnight culture into fresh LB in 96-well plates, in working volumes of 200 μ L, with 2-fold dilutions of antibiotic across wells. The MIC was determined as the minimum concentration at which no visible growth occurred overnight (OD₆₀₀ < 0.1). A summary of all MIC values thus determined is provided in Table S1, and all measurements were performed in biological duplicate.

419 4.10 Mechanical model of bacterial cell lysis

The model. This work builds on a model of bacterial cell lysis introduced by some of us (Wong and 420 Amir, 2019), showing how it can be extended to yield predictions for the perturbations considered in this 421 work. Our model is different from a previous model by Daly et al., (Daly et al., 2011) due to our focus on 422 stretching energies, and not bending energies, as the main source of strain in the cell envelope; additional 423 comparisons between these models are detailed in ref. (Wong and Amir, 2019). Here, for completeness, the 424 model is described in full, then extended. We model the cell wall, inner membrane, and outer membrane 425 of a Gram-negative cell as thin, homogeneous, elastic layers in contact. Unlike the rigid cell wall, the 426 membranes are fluid and hence free to change their reference configurations under the constraint of fixed 427 reference areas. The free energy of the cellular envelope and the volume it encloses is 428

$$\mathcal{F} = E_{\text{strain}}^w + E_{\text{strain}}^i + E_{\text{strain}}^o - TS, \tag{1}$$

where the superscripts w, i, and o denote cell wall, inner membrane, and outer membrane quantities, 429 430 respectively, E_{strain} is the elastic strain energy, T is the temperature, and S is the entropy of mixing water and solutes. Assuming only water molecules outside the cell for simplicity, $S = -k(n_s \ln x_s + n_w \ln x_w)$, 431 where k is Boltzmann's constant, x_s and x_w are the number fractions of solute and water molecules, 432 433 respectively, and n_s and n_w are the numbers of solute and water molecules, respectively. Note that the turgor pressure is defined as p = kTC, where C is the solute concentration, and that the origin of turgor is 434 entropic. Furthermore, we do not consider growth of the cell due to the timescales of interest in this work. 435 436 Below, we neglect the hemispherical poles of the cell for simplicity and consider only the cylindrical bulk.

To describe how the cell envelope reacts to the turgor pressure, we first note that, for characteristic parameter values relevant to E. coli (Table S2), the stretching energy will dominate the bending energy in $E_{\rm strain}$, as is typical for thin shells. We assume an orthotropic constitutive relation for the cell wall, consistent with evidence for a larger Young's modulus in the circumferential direction than that in the axial direction (Deng et al., 2011; Lan et al., 2007), but note that the main predictions relevant to this work, as detailed below, do not depend on this assumption. As the membranes are assumed to be fluid, their

Running Title Wong et al.

stretching is characterized by their area stretch moduli. \mathcal{F} can then be reexpressed as

$$\mathcal{F} = -TS + \frac{1}{2} \int \frac{(\sigma_{xx}^w)^2}{Y_x^w} + \frac{(\sigma_{yy}^w)^2}{Y_y^w} - \left(\frac{\nu_{xy}^w}{Y_x^w} + \frac{\nu_{yx}^w}{Y_y^w}\right) \sigma_{xx}^w \sigma_{yy}^w dA^w + \sum_{\alpha \in \{i,o\}} \frac{K_a^\alpha}{2} \int (u_{xx}^\alpha + u_{yy}^\alpha)^2 dA^\alpha. \quad (2)$$

- Here $(Y_x^w, Y_y^w, \nu_{xy}^w, \nu_{yx}^w)$ are the two-dimensional Young's modulus and Poisson's ratio of the cell wall in the axial and circumferential (x and y) directions, K_a^{α} is the area stretch modulus, u denotes in-plane
- 445
- strains, σ denotes in-plane stresses, and dA^{α} denotes an area element. α represents an index: the inner 446
- and outer membranes are represented by $\alpha = i$ and $\alpha = o$, respectively, while the cell wall is represented 447
- by $\alpha=w$. Due to membrane fluidity, $u_{xx}^{\alpha}=u_{yy}^{\alpha}$ for $\alpha\in\{i,o\}$ when $\mathcal F$ is minimized (Wong and Amir, 448
- 2019). Furthermore, it is straightforward to show that u_{xx}^{α} does not vary with membrane position, so that 449
- the membrane stresses are isotropic and homogeneous (Wong and Amir, 2019). 450
- For simplicity, we do not distinguish between the inner and outer membranes $(K = K_a^i = K_a^o)$, so that 451
- all equations that follow hold for either membrane. We note here that the analogous free energy of a cell 452
- 453 envelope comprising only a cytoplasmic membrane (indexed by i) can be written similarly to Eq. (2). We
- find that it is equivalent to Eq. (2) under the mapping $K \mapsto K/2$ and $\sigma^i + \sigma^o \mapsto \sigma^i$. Hence, the case of a 454
- single membrane, as is relevant for Gram-negative cells without outer membranes or Gram-positive cells, 455
- can be readily accommodated by the considerations below. 456
- To determine the stresses in the cellular envelope before cell wall defect formation, it suffices to determine 457
- $\sigma = \sigma_{xx}^{\alpha} = \sigma_{yy}^{\alpha} = 2Ku_{xx}^{\alpha} = 2Ku_{yy}^{\alpha}$ for $\alpha = i, o$, from which the stresses in the cell wall follow by force 458
- balance. As shown previously (Wong and Amir, 2019), a direct application of force balance yields

$$\sigma = \frac{K(-(\mathcal{A} - 2\pi r_0^w L_0^w)Y_x^w Y_y^w + kT n_s (2Y_x^w (1 - \nu_{yx}^w) + Y_y^w (1 - \nu_{xy}^w))}{2\pi r_0^w L_0^w (2K(Y_x^w (1 - \nu_{yx}^w) + Y_y^w (1 - \nu_{xy}^w)) + Y_x^w Y_y^w)}.$$
(3)

- Here $\mathcal{A} = \gamma \times 2\pi r_0^w L_0^w$ is the (inner or outer) membrane reference area, with γ denoting the reference
- membrane surface area ratio as compared to the cell wall, and r_0^w and L_0^w are the reference radius and 461
- length of the cell wall. Assuming the material parameters of the cellular envelope summarized in Table S2, 462
- we solved Eq. (3) to determine the stresses of the unbulged state, as shown in Figure S2. We performed 463
- these calculations for (1) the physiological (wild-type) case; (2) a case in which the turgor was reduced 464
- $(n_s = 4.7 \times 10^7)$; and (3) a case in which there is no outer membrane, as discussed above. These calculations 465
- were supported by numerically minimizing \mathcal{F} , as previously described (Wong and Amir, 2019). 466
- As the timescale of membrane lipid synthesis (tens of minutes, (Emiola et al., 2015)) is anticipated to 467
- be longer than the timescale of bulging (seconds; see Figure 1D), we assume the membrane reference 468
- surface areas to remain unchanged, so that bulging corresponds to a quasi-equilibrium state in which the 469
- membrane reference surface areas limit bulge expansion. As shown previously (Wong and Amir, 2019), 470
- determining the equilibrium conformation of the cell envelope once a circular cell wall defect A of radius 471
- r_d is introduced amounts to solving a single, transcendental equation. In particular, the bulged conformation 472
- will exhibit a partially-subtended, spherical bulge (B; Figure S2A) whose subtended angle, θ , is determined
- by the following *bulging equation*:

$$\mathcal{A} = 2\pi r_0^w L_0^w - \pi r_d^2 \left(1 - \frac{2}{1 + \cos \theta} \right) + \frac{3kT n_s}{4K Y_x^w Y_y^w} \times \frac{\Phi(\theta)}{3(r_0^w)^2 L_0^w \sin^3 \theta + r_d^3 (2 + \cos \theta) (\cos \theta - 1)^2}, \tag{4}$$

where
$$\Phi(\theta) = 2r_0^w L_0^w (2Kr_0^w \sin^3\theta (2Y_x^w (1 - \nu_{yx}^w) + Y_y^w (1 - \nu_{xy}^w)) - r_d \sin^2\theta (Y_x^w Y_y^w + 2K(Y_x^w (1 - \nu_{yx}^w) + Y_y^w (1 - \nu_{xy}^w))) - r_d^3 Y_x^w Y_y^w \tan^2(\theta/2) \sin^2\theta.$$

Assuming the material parameters of the cellular envelope summarized in Table S2, we solved Eq. (4) to determine the stresses and geometry of the bulged state, as shown in Figure S2C, for (1) the physiological (wild-type) case; (2) a case in which the turgor was reduced; and (3) a case in which there is no outer membrane. These calculations were again supported by numerically minimizing \mathcal{F} , as above. The bulge radius R was found by the relation $R = r_d \sin \theta$ (Figure S2A). Note that the model predicts bulging to occur, in principle, for any finite value of r_d ; nevertheless, for values much smaller than \sim 4-10 nm, the thickness of a lipid bilayer, the membrane cannot extrude through the cell wall defect and form a bulge. Accordingly, we anticipate the model to be physically accurate for large enough defect sizes, $r_d \gtrsim 10$ nm.

For the characteristic defect sizes considered here $(r_d \sim 1~\mu\text{m})$, the salient assumption of our model is that bulging corresponds to a quasi-equilibrium state in which force balance holds. We therefore sought to probe the implications of force balance on lysis dynamics. As we have assumed the inner and outer membranes to possess similar material properties, the model predicts the membranes to be similarly load-bearing and collectively resist stresses proportional to pR/2 (Figure S2C) in the bulge. The strains collectively resisted are then pR/(4K). Assuming a fixed yield strain of the membranes then implies that, if the turgor pressure is reduced by a factor of two, then the yield bulge radius will be increased by a factor of two.

Increased membrane tension after bulging. Our model suggests that the increase in membrane tension after bulging is sufficient to trigger MSCs in many cells, as we explain next. According to the assumptions of force balance and identical membrane material properties in our model, the stress in each membrane at the time of lysis is $pR_{\text{yield}}/4$, where R_{yield} is the the yield bulge radius. For characteristic parameter values, our model also predicts physiological membrane stresses—that is, stresses in the unbulged state—of approximately 5 mN/m (Eq. (3) and Figure S2B). As the cellular volume remains essentially unchanged after bulging, increasing on average by <10% (Figure S6A), the same turgor pressure and a typical value of 0.9 μ m for R_{yield} (Figure 2E of the main text) predicts a mean membrane stress of approximately 11 mN/m at lysis. The right tail of the yield radii distribution (\sim 10% of cells) corresponds to increased tensions of >20 mM/m, illustrating substantial variability between cells. For comparison, the MSCs MscS and MscL gate upon an increase in membrane tension in the range of 5-15 mN/m (Buda et al., 2016). The stress differential of >6 mN/m predicted by our model therefore suggests gating in a large fraction (\sim 40%) of cells exhibiting yield bulge radii equal to, or greater than, 0.9 μ m.

Dependence of bulge size on cell width. As stated in the main text, we may consider a simple case of Eq. (4) in which $Y_x^w = Y_y^w = Y$ and we neglect Poisson's effect ($\nu = \nu_{xy}^w = \nu_{yx}^w = 0$). Accurate to the first order in r_d/R , the solution of Eq. (4) reduces to the following:

$$\theta \approx \frac{r_d}{R}, \quad R \approx \frac{6kTn_sKr_0^w - 4(\gamma - 1)KY\pi(r_0^w)^2L_0^w}{kTn_s(4K + Y)}.$$
 (5)

For the parameters values of interest (Table S2), the second term in the numerator of R in Eq. (5) is dominated by the first; we therefore write

$$R \approx \frac{6kTn_sKr_0^w}{kTn_s(4K+Y)} = \frac{6Kr_0^w}{4K+Y}.$$
 (6)

Thus, Eq. (6) reveals a simple dependence of the bulge radius on the cell width: it predicts wider cells to yield larger bulges, with the subtended angle being determined by the ratio of cell wall hole radius to

bulge radius. We note that wider mreB-titratable cells exhibit larger bulge radii, R, and similar values of

subtended angles, θ , to thinner cells; this observation suggests larger values of the defect radius relative to

thinner cells, consistent with the measurements shown in Figure S8F.

4.11 Transport model for solute outflow

515

522

523

524

525

526

527

528

529

Change in cellular turgor and volume due to MSC gating. To better understand the effect of MSCs on cellular turgor, we extended our biophysical model of cell envelope mechanics to predict the timescale of turgor loss due to MSC gating. A similar model, where the leakage of solutes arises from membrane defects, has been developed by some of us (Wong et al., 2021). As in Eq. (1), we model the Gram-negative bacterial cell envelope as the combination of an elastic shell (the cell wall) sandwiched between two fluid membranes (the inner and outer membranes).

We assume that MSC gating is well described by the addition of nanoscale gaps of characteristic diameter \sim 3 nm in the membrane (Buda et al., 2016; Naismith and Booth, 2012). Thus, we model MSCs as holes with characteristic radius $r_c \approx 1.5$ nm, which is smaller than the thickness of a lipid bilayer, \sim 4-10 nm. We next consider the electrochemical potential across the membrane, which comprises contributions due to the membrane potential and the chemical potential of cytoplasmic solutes. In *E. coli*, physiological estimates of the membrane potential are approximately -100 mV (Felle et al., 1980; Lo et al., 2007; Ramos et al., 1976). In the case where the cellular turgor is predominantly generated by a concentration imbalance of an ion, the chemical potential, E, can be determined by the Nernst equation,

$$E = \frac{kT}{ze} \ln \left(\frac{C_i}{C_o}\right),\tag{7}$$

where e is the elementary electric charge, z is the ion charge, and C_i and C_o are the concentrations of ions inside and outside the cell, respectively (Benarroch and Asally, 2020). We assume a typical cellular turgor 531 pressure of ~ 0.5 atm (Table S2) corresponding to a solute concentration difference of ~ 25 mM, and that 532 533 K^+ ions, for which z=1, dominate the composition of all solutes in the cell, consistent with estimates of 534 ion composition in E. coli (Milo and Phillips, 2015). We further assume an intracellular K⁺ concentration 535 of \sim 25 mM, qualitatively consistent with typical estimates of 30-300 mM (Milo and Phillips, 2015). Eq. (7) then implies a chemical potential of $E \sim 140$ mV, with larger predicted values for larger turgor pressures. 536 As the membrane potential is smaller than, or comparable to, the predicted chemical potential and is also 537 538 expected to collapse rapidly after channel gating due to inflow of Na⁺ and H⁺ (Lo et al., 2007; Booth, 2014), for simplicity, we consider the case in which solute outflow is driven predominantly by the chemical 539 potential below. 540

For defects of characteristic diameter ~3 nm as assumed above, the hydrodynamic outflow of cytoplasmic contents—anticipated here to comprise mainly of water containing osmolytes—from inside to outside the cell is laminar and well described by Poiseuille flow, so that the volumetric flow rate is

$$Q = \frac{\Delta P A^2}{8\pi\mu L_c}. (8)$$

Here ΔP is the pressure drop inside and outside the cell, $A=\pi r_c^2$ is the hole area, L_c is the hole length, and μ is the viscosity of the medium. Eq. (8) is anticipated to be valid for describing the flow of osmolytes in water through high conductance, non-specific channels such as MscL and MscS, as reviewed previously (Haswell et al., 2011); we do not consider flow of ions through low conductance, selective ion channels here. We further note that, due to the entropic origin of turgor, p decreases with flow of solutes outside the

cell and flow of water into the cell through the semi-permeable cell membranes. In turn, MSCs may stop gating due to there being less mechanical strain in the cell membranes.

For characteristic parameter values, as summarized in Table S2, we find that, at the start of flow, $Q \approx 10^{-21} \,\mathrm{m}^3/\mathrm{s}$. Assuming this flow rate to be constant in time and a characteristic number of $\sim 100 \,\mathrm{gated}$ MSCs of all types in the cell—consistent with census estimates for MscL (Chure et al., 2018; Bialecka-Fornal et al., 2012)—a simple estimate shows that a flow comparable to the entire cellular volume out of the cell occurs on a timescale of $\sim 100 \,\mathrm{s}$, a timescale comparable to the mean bulge lifetimes observed in our lysis experiments.

We now perform a more detailed analysis, taking into account the decrease of turgor and cell volume with flow of solutes outside the cell. A characteristic value of the diffusion constant of ions in water is $D \approx 10^{-9} \text{ m}^2/\text{s}$ (Cussler, 1997), so that a typical root-mean-square distance traveled by an ion per second is $10 \mu\text{m}$. Accordingly, we assume solutes to be significantly diluted once outside the cell, so that $\Delta P = p$, the turgor pressure of the cell. Viewing n_s , p, Q, and the cell volume, V, as time-dependent quantities that change with flow of solutes out of the cell, we therefore write:

$$Q(t) = \frac{\pi p(t)r_c^4}{8\mu L_c}, \quad p(t) = \frac{kTn_s(t)}{V(t)}, \quad \frac{dn_s(t)}{dt} = -\frac{\mathcal{N}Q(t)n_s(t)}{V(t)}, \tag{9}$$

where \mathcal{N} is the number of gated MSCs. We note here that r_c is assumed to be constant over time, in contrast to our previous model examining membrane defects (Wong et al., 2021). It therefore remains to determine V(t). As mentioned in the main text, we will first consider the analytically tractable case of a cell with no bulges, then verify that the theoretical predictions are quantitatively similar in the case of a cell with a bulge.

Elastic determination of the cellular volume. Due to the possibility of water flow into the membrane as the number of solutes are modulated, we hypothesize the cellular volume to be determined by the equilibration of the elastic strain energies in Eq. (1). In particular, given the turgor pressure, p(t), the cell envelope is free to change its dimensions to minimize the free energy. This timescale separation is supported by the following estimate. The bulk flow of water through the cell membranes is described by

$$\frac{dV_{\text{water}}}{dt} = L_p A_{\text{cell}} p,\tag{10}$$

where L_p is the hydraulic conductivity of the membranes and $A_{\rm cell}$ is the total membrane surface area (Sperelakis, 1995). For characteristic values of these parameters, as summarized in Table S2, we find that a typical \sim 40% change in cellular volume occurs within \sim 1 s. Hence, for the timescale of interest (\sim 1 s) here, we find that water flow should indeed occur fast enough for the cell to be in equilibrium.

577

578

579

580

581

582

583

We therefore determine V(t) by finding the elastic stresses in the equilibrium conformation. For this, we resort to a linear theory and assume, as above, a linear-elastic, isotropic cell wall, with reference radius and lengths r_0^w and L_0^w , respectively, and (two-dimensional) Young's modulus and Poisson's ratio Y^w and ν^w , respectively. Moreover, as before, we view the two membranes as materially identical and fluid in-plane, so that their stretching is governed by their area-stretch modulus, $K = K^i = K^o$, and reference surface area ratio, $\gamma = A_0^i/A_0^w = A_0^o/A_0^w$, where A_0^w is the reference cell wall surface area, and A_0^i and A_0^o are the inner and outer membrane reference surface areas, respectively (Wong and Amir, 2019). The free energy

of Eq. (1) can then be expressed as

591

592

593

594

595

596

597

598

$$\mathcal{F} = \frac{1}{2Y^w} \int [(\sigma_{xx}^w)^2 + (\sigma_{yy}^w)^2 - 2\nu^w \sigma_{xx}^w \sigma_{yy}^w] dA^w + 2K \int (u^i)^2 dA^i + 2K \int (u^o)^2 dA^o - TS, \quad (11)$$

where the integrals are over the deformed surface areas, σ^w_{xx} and σ^w_{yy} are cell wall stresses, and u^i and u^o are inner and outer membrane strains, respectively. As detailed in the previous section (*Mechanical Model of Bacterial Cell Lysis*), the form of E^i_{strain} and E^o_{strain} in Eq. (11) arises from the fluid in-plane nature of the membranes; it follows from this that the membrane strains and stresses are isotropic and spatially homogeneous (Wong and Amir, 2019). As the cell wall is cylindrical, its strains and stresses will also be spatially homogeneous, but not necessarily isotropic.

Depending on the values of γ , K, and p, we note that, in general, the deformed membrane dimensions can be different from each other and those of the cell wall: in the limit of small $0 < \gamma \ll 1$ and $p/K \ll 1$, for instance, the free energy is minimal when the inner membrane forms a spherical vesicle inside the cell and the cell wall and outer membrane bear no load. However, we may anticipate a parameter regime in which all envelope layers bear some load (below). Then, by symmetry of the inner and outer membranes, $u=u^i=u^o$ and the membrane stresses $\sigma=\sigma^i=\sigma^o$; moreover, these quantities will all be nonzero. As detailed in the previous section, the mechanical stresses will be related to the strains by the following constitutive relations (Wong and Amir, 2019):

$$\sigma_{xx}^{w} = \frac{Y^{w}}{1 - (\nu^{w})^{2}} (u_{xx}^{w} + \nu^{w} u_{yy}^{w}), \quad \sigma_{yy}^{w} = \frac{Y^{w}}{1 - (\nu^{w})^{2}} (u_{yy}^{w} + \nu^{w} u_{xx}^{w}), \quad \sigma = 2Ku.$$
 (12)

Here, the cell wall strains u_{xx}^w and u_{yy}^w correspond to the stresses σ_{xx}^w and σ_{yy}^w . Furthermore, the linear strain-displacement relations are

$$u_{xx}^{w} = \frac{r - r_{0}^{w}}{r_{0}^{w}}, \quad u_{yy}^{w} = \frac{L - L_{0}^{w}}{L_{0}^{w}}, \quad u = \frac{A^{i} - A_{0}^{i}}{2A_{0}^{i}} = \frac{A^{o} - A_{0}^{o}}{2A_{0}^{o}}, \tag{13}$$

where r and L are the deformed cell wall radius and length, respectively. Assuming that the membranes share the same deformed radius and length, we substitute Eqs. (12) and (13), as well as the relation $n_w = \pi r^2 L/m_w$, where m_w is the volume occupied per water molecule, into Eq. (11). From this, we find that \mathcal{F} can be rewritten as a function of two unknowns, r and L, and several parameters including the elastic constants, γ , and n_s . Hence, we will minimize \mathcal{F} over r and L, from we determine all associated elastic quantities.

As mentioned above, we anticipate that, for typical cells, the membrane reference areas will be similar 607 to that of the cell wall, so that $|\gamma - 1| \ll 1$ (Wong and Amir, 2019). Furthermore, we anticipate all 608 cell envelope layers to be load-bearing and in contact in the deformed state, so that we may suppose a 609 common value of the deformed cell length and radius among all envelope layers; these may be expressed as 610 $L = L_0^w + \delta L$ and $r = r_0^w + \delta r$, where δL and δr are viewed as small relative to L_0^w and r_0^w , respectively. 611 We note that the general case in which this assumption is not satisfied involves a minimization of the free 612 energy over additional variables describing the membrane geometries (Wong et al., 2017), which makes 613 deriving analytic expressions for σ^w_{xx} and σ^w_{yy} more complicated than presented here. Next, we make the 614 following small-variable assumptions: $n_s/n_w \ll 1$ and $\delta r/r, \delta L/L = O(\varepsilon)$, where $\varepsilon \ll 1$, consistent with 615 the linear theory. In particular, since characteristic parameter values give $n_s/n_w \approx 10^{-4}$ and we may expect $|\gamma-1|\approx 0.01$ and $u,u^w_{xx},u^w_{yy}\approx 0.01$ (Table S2), we will expand $\mathcal F$ to first order in n_s about 0,

second order in ε about 0, and second order in γ about 1. Doing so, and analytically solving for the values of δL and δr which minimize \mathcal{F} , upon substitution of the solution into Eqs. (12) and (13) we find

$$\sigma_{xx}^{w} = \frac{(\gamma - 1)KY^{w}}{Y + 2K(1 - \nu^{w})} + \frac{kTn_{s}(K - K\nu^{w} + 2Y^{w})}{2\pi r_{0}^{w}L_{0}^{w}[2K(1 - \nu^{w}) + Y^{w}]}$$

$$+O(\varepsilon^{2}) + O\left[\left(\frac{n_{s}}{n_{w}}\right)^{2}\right] + O((\gamma - 1)^{2}) + O((\gamma - 1)\varepsilon) + O\left(\frac{(\gamma - 1)n_{s}}{n_{w}}\right) + O\left(\frac{\varepsilon n_{s}}{n_{w}}\right).$$
(14)

Accurate to the same order, we have

$$\sigma_{yy}^{w} = \frac{(\gamma - 1)KY^{w}}{Y^{w} + 2K(1 - \nu^{w})} + \frac{kTn_{s}(K - K(\nu^{w})^{2} + Y^{w})}{2\pi r_{0}^{w}L_{0}^{w}[2K(1 - \nu^{w}) + Y^{w}]}, \quad \sigma = \frac{K[3kTn_{s}(1 - \nu^{w}) - 2\pi r_{0}^{w}L_{0}^{w}(\gamma - 1)Y^{w}]}{4\pi r_{0}^{w}L_{0}^{w}[2K(1 - \nu^{w}) + Y^{w}]}.$$
(15)

- It is straightforward to verify that $\sigma_{xx}^w + 2\sigma = \frac{kTn_s}{\pi r_0^w L_0^w}$ and $\sigma_{yy}^w + 2\sigma = \frac{kTn_s}{2\pi r_0^w L_0^w}$, so that Laplace's law (Wong and Amir, 2019) is satisfied. We note here that the stresses of Eqs. (14) and (15) do not vanish 621
- 622
- when $n_s = 0$, due to the simplifying assumption of a common value of the deformed cell length and radius 623
- among all envelope layers. When $n_s = 0$, the membranes are free to assume dimensions that minimize 624
- their stretching energies and, in general, the assumption of a common value of the deformed cell length 625
- and radius among all envelope layers no longer holds. However, for characteristic values of n_s relevant 626
- 627 to E. coli, as considered in this work, we have previously shown that this assumption is valid (Wong and
- Amir, 2019). This assumption then results in the simplified expressions for the stresses given by Eqs. (14) 628
- and (15). 629
- Finally, by viewing the stresses in Eqs. (14) and (15) as functions of time through their dependence on 630
- $n_s = n_s(t)$ and finding the corresponding time-dependent strains through the linear constitutive relations 631
- of Eq. (12), we can write a closed-form expression for V(t) as: 632

$$V(t) = \pi(r_0^w)^2 L_0^w [1 + 2u_{xx}^w(t) + u_{yy}^w(t)].$$
(16)

- Henceforth, all equalities will be accurate to the orders shown in Eq. (14). 633
- The dynamical equation. Iteratively substituting Eqs. (12)-(16) into Eq. (9), we find that a single 634 635 equation governs the dynamics of solute flow which, in turn, determines all other quantities:

$$\frac{dn_s(t)}{dt} = -\frac{\pi \mathcal{N}kTn_s^2(t)r_c^4(Y^w)^2(Y^w + 2K(1-\nu^w))^2}{2\mu L_d(r_0^w)^2[2\pi r_0^w L_0^w Y^w(Y^w + K(1-\nu^w)(3\gamma-1)) + kTn_s(t)(K-K(\nu^w)^2 + Y^w(5-4\nu^w))]^2},$$

- where $n_s(t=0) = n_s^0$, the initial number of solutes inside the cell. We numerically solved this equation for the parameter values of interest (Table S2). 637
- Timescales of solute flow and increases in bulge stress. Solving the dynamical Eq. (17) numerically for 638 the parameter values summarized in Table S2, we find that the model predicts a gradual decrease in turgor 639 on the timescale of ~ 100 s, followed by accompanying decreases in volume (Figure S3). Importantly, we 640 find that this decrease in turgor is insufficient to overcome the increase in membrane stresses due to bulge 641 growth: based on our experimental observations that the mean bulge radius is $\sim 1 \mu m$ after ~ 200 s (Figures 642 1 and 2 of the main text), we find that a typical bulge radius growth rate of 0.005 μ m/s is large enough so that 643 the corresponding estimate of bulge stress, $\sigma = p(t)R(t)/2$, is monotonically increasing in time (Figure 644 S3), where p(t) is determined by the solution of Eq. (17) and R(t) is taken to be $R(t) = 0.005 \ \mu \text{m/s} \times t$ 645

as a phenomenological approximation to our observations. We note here that heterogeneous dynamics in R(t), as would be expected if the bulge does not grow constantly in time, would lead to different predicted behaviors of σ .

While we have modeled cells without bulges, we note that considering the bulge geometry would make an expression of the form Eq. (17) intractable to obtain, as the transcendental bulging equation (Eq. (4)) would need to be solved to obtain the stresses of Eqs. (14) and (15). Nevertheless, we have previously shown that numerical solutions of the bulging equation indicate the cell volume of a bulged cell to be approximately equal to that on an unbulged cell (Wong and Amir, 2019). As the model predictions are robust to variations in V(t) (Figure S3), we expect that the inclusion of a bulge to the analysis has a limited effect on the model predictions. In confirmation of this, we numerically solved Eq. (9) in the case where V(t) is determined by the bulging equation, and observed that the model predictions were, as expected, quantitatively similar to the unbulged case (Figure S4A).

In conclusion, our modeling results demonstrate how MSCs may fail to resist lysis. Furthermore, these results suggest that, while solute outflow may decrease turgor in cells, the turgor decrease is counteracted by bulge growth, leading to increasing mechanical stresses until the cell lyses.

Comparison with cells under hypoosmotic shock. We summarize the main differences between our model and that previously developed for cells under hypoosmotic shock (Buda et al., 2016). In both cases, the model predicts the outflow of solutes in response to the gating of MSCs; for bulged cells, however, our model suggests that the outflow of solutes is insufficient to decrease the mechanical stresses in the bulge, since decreases in the turgor pressure (p) are compensated for by increases in the bulge radius (R) such that the mechanical stresses in the bulge (equal to pR/2) increases in time (Figure S3). In contrast, in experiments involving hypoosmotic shocks, cells do not exhibit bulges and the mechanical stresses in the cell envelope are proportional to pr, where r is the cell radius. As r does not significantly increase in time and p decreases with solute outflow, the mechanical stresses in the cell envelope decrease, instead of increase, in time. This difference is further illustrated in Figure S4B, in which we plot the bulge areal strain, defined as the quantity $2u = (A^i - A_0^i)/A_0^i = (A^o - A_0^o)/A_0^o = p(t)R(t)/4K$, after MSC gating; note that a factor of 2 enters in the denominator due to the presence of two membranes. For comparison, the membrane areal strain of a cylindrical cell after MSC gating, but without bulging, is also plotted in Figure S4B.

4.12 Generality of model assumptions: osmotic nature of the periplasm

In our model, we have assumed that the turgor pressure is generated by solutes in the cytoplasm (Hussain et al., 2018; Wong and Amir, 2019; Wong et al., 2021) and exerts a force on all three layers of the Gramnegative bacterial cell envelope. This assumption is consistent with viewing the periplasm as an effectively rigid body. We have previously suggested (Hussain et al., 2018) that a case in which the cytoplasm is isoosmotic with the periplasm (Sochacki et al., 2011; Erickson, 2017, 2021), such that the OM is effectively rigid and the only load-bearing layer of the cellular envelope, is inconsistent with the mechanical stability of the periplasm because the bending energies of the membranes in Eq. (1) are smaller for cylindrical shapes of larger radius: thus, in rod-like cells with sufficient IM surface area, the IM is predicted to press against the cell wall and OM and squeeze out any isoosmotic periplasmic space (see (Hussain et al., 2018) for a detailed discussion). Nevertheless, this case can be accommodated in our model by (1) setting K=0 and the elastic moduli of the cell wall, Y^w , to be that of the rigid OM in the cylindrical bulk of the cell, and (2) viewing K as the area-stretch modulus of the cell wall-decoupled, fluid OM in the bulge. As a previous study has indicated the presence of cytoplasm in membrane bulges (Yao et al., 2012), our model suggests that the formation of a membrane bulge after β -lactam treatment depends on the untethering of proteins

anchoring the IM and OM to the cell wall: such proteins may include transmembrane cell wall synthases

- 691 including the Rod complex, Braun's lipoprotein, and OmpA (van Teeffelen and Renner, 2018; Silhavy
- 692 et al., 2010; Movva et al., 1980).
- We note that, in both cases, the bulge stresses are identical and equal to $\sigma = p(t)R(t)/2$. This observation
- 694 indicates that the prediction of turgor pressure as a driver of lysis applies to both cases. Furthermore,
- 695 in the case of an isoosmotic periplasm, the dynamical equation for solute outflow out of a rod-like cell,
- 696 corresponding to Eq. (17), is

$$\frac{dn_s(t)}{dt} = -\frac{\pi \mathcal{N}kTr_c^4(Y^w)^4 n_s(t)^2}{2\mu L_d(r_0^w)^2 [2\pi r_0^w L_0^w(Y^w)^2 + kTn_s(t)Y^w(5 - 4\nu^w)]^2},$$
(18)

697 where r_0^w, L_0^w, Y^w , and ν^w describe quantities relevant to the effectively rigid outer membrane. For

- 698 characteristic parameter values relevant to E. coli (Table S2), the predictions of Eq. (18) are quantitatively
- 699 similar to those of Eq. (17). Thus, we anticipate that the model predictions for the effects of hyperosmotic
- 700 shock and MSC gating on lysis are qualitatively similar between both cases. We anticipate that further
- 701 studies will better discriminate between these two sets of model assumptions by clarifying the osmotic
- 702 nature of the periplasm.

5 CONFLICT OF INTEREST STATEMENT

703 The authors declare that the research was conducted in the absence of any commercial or financial

704 relationships that could be construed as a potential conflict of interest.

6 AUTHOR CONTRIBUTIONS

- 705 F.W., A.A., and L.D.R. conceived the project. F.W., S.W., C.L., T.P., E.C.G., A.A., and L.D.R. designed
- 706 research. F.W., S.W., R.H., S.H., O.A., H.Z., and L.D.R. performed research. All authors analyzed data.
- 707 F.W., S.W., T.P., E.C.G., A.A., and L.D.R. wrote the paper with the assistance of all authors.

7 FUNDING

- 708 F.W. was supported by the James S. McDonnell Foundation and a National Science Foundation (NSF)
- 709 Graduate Research Fellowship under grant no. DGE1144152. S.H. was supported by the Darwin Trust. S.H.
- and T.P. were supported by the Industrial Biotechnology Innovation Centre (IBioIC) and the Biotechnology
- 711 and Biological Sciences Research Council UK via the Crossing Biological Membrane Network in Industrial
- 712 Biotechnology and Bioenergy (CBMNet). E.C.G. was supported by the National Institutes of Health under
- 713 grant no. DP2AI117923-01, a Smith Family Award, and a Searle Scholar Fellowship. A.A. was supported
- 514 by an NSF CAREER Award under grant no. 1752024. F.W. and A.A. were supported by the Kavli Institute
- 715 for Bionano Science and Technology at Harvard and the Materials Research and Engineering Center at
- 716 Harvard under grant no. DMR-1420570. E.C.G., A.A., and L.D.R. were supported by the Volkswagen
- 717 Foundation.

8 ACKNOWLEDGMENTS

- 718 We thank Sue Sim, Anastasiya Yakhnina, Thomas G. Bernhardt, Douglas B. Weibel, and members of the
- 719 Weibel lab for providing the assorted E. coli strains summarized in Table S1, Georgia Squyres and Yingjie
- 720 Sun for microscopy assistance, Sven van Teeffelen, Gizem Özbaykal, and Namiko Mitarai for discussions,
- and the Harvard Department of Statistics Consulting Service for helpful feedback.

9 SUPPLEMENTAL DATA

Supplementary Information includes eight figures, three tables, six movies, and Supplementary References.

10 DATA AVAILABILITY STATEMENT

723 The data that support the findings of this study are available from the corresponding authors upon request.

REFERENCES

- Aidelberg, G., Towbin, B. D., Rothschild, D., Dekel, E., Bren, A., and Alon, U. (2014). Hierarchy of
- non-glucose sugars in Escherichia coli. BMC Syst. Biol. 8, 133
- 726 Baba, T., Ara, T., Hasegawa, M., Takai, Y., Okumura, Y., Baba, M., et al. (2006). Construction of
- 727 Escherichia coli K-12 in-frame, single-gene knockout mutants: the Keio collection. Mol. Syst. Biol. 2,
- 728 2006.0008. doi:10.1038/msb4100050
- 729 Bean, G. J., Flickinger, S. T., Westler, W. M., McCully, M. E., Sept, D., Weibel, D. B., et al. (2009). A22
- disrupts the bacterial actin cytoskeleton by directly binding and inducing a low-affinity state in MreB.
- 731 *Biochemistry* 48, 4852–4857
- 732 Benarroch, J. M. and Asally, M. (2020). The microbiologist's guide to membrane potential dynamics.
- 733 *Trends Microbiol.* 28, 304–314
- 734 Bertani, G. (1951). Studies on lysogenesis I: the mode of phage liberation by lysogenic Escherichia coli. J.
- 735 Bacteriol. 62, 293–300
- 736 Bertani, G. (2004). Lysogeny at mid-twentieth century: P1, P2, and other experimental systems. J.
- 737 Bacteriol. 186, 595–600
- 738 Bialecka-Fornal, M., Lee, H. J., DeBerg, H. A., Gandhi, C. S., and Phillips, R. (2012). Single-cell census
- of mechanosensitive channels in living bacteria. *PLoS ONE* 7, 0033077
- 740 Bialecka-Fornal, M., Lee, H. J., and Phillips, R. (2015). The rate of osmotic downshock determines the
- survival probability of bacterial mechanosensitive channel mutants. J. Bacteriol. 197, 231–237
- 742 Blair, J. M. A., Webber, M. A., Baylay, A. J., Ogbolu, D. O., and Piddock, L. J. V. (2015). Molecular
- mechanisms of antibiotic resistance. *Nat. Rev. Microbiol.* 13, 42–51
- 744 Boer, M., Anishkin, A., and Sukharev, S. (2011). Adaptive MscS gating in the osmotic permeability
- response in *E. coli*: the question of time. *Biochemistry* 50, 4087–4096
- 746 Booth, I. R. (2014). Bacterial mechanosensitive channels: progress towards an understanding of their roles
- in cell physiology. Curr. Opin. Microbiol. 18, 16–22
- 748 Buda, R., Liu, Y., Yang, J., Hegde, S., Stevenson, K., Bai, F., et al. (2016). Dynamics of Escherichia
- 749 *coli*'s passive response to a sudden decrease in external osmolarity. *Proc. Natl. Acad. Sci. USA* 113,
- 750 E5838–E5846
- 751 Bush, K. and Bradford, P. A. (2016). β -lactams and β -lactamase inhibitors: an overview. *Cold Spring*
- 752 *Hard. Perspect. Med.* 6, a025247
- 753 Cabeen, M. T. and Jacobs-Wagner, C. (2005). Bacterial cell shape. Nat. Rev. Microbiol. 3, 601–610
- 754 Cayley, D. S., Guttman, H. J., and Record, M. T. (2000). Biophysical characterization of changes in
- amounts and activity of *Escherichia coli* cell and compartment water and turgor pressure in response to
- 756 osmotic stress. *Biophys. J.* 78, 1748–1764
- 757 Cetiner, U., Rowe, I., Schams, A., Mayhew, C., Rubin, D., Anishkin, A., et al. (2017). Tension-activated
- channels in the mechanism of osmotic fitness in *Pseudomonas aeruginosa*. J. Gen. Physiol. 149,
- 759 595–609
- 760 Centers for Disease Control and Prevention (2019). Antibiotic resistance threats in the United States, 2019

Chabanon, M., Ho, J. C. S., Liedberg, B., Parikh, A. N., and Rangamani, P. (2017). Pulsatile lipid vesicles
 under osmotic stress. *Biophys. J.* 112, 1682–1691

- 763 Chikada, T., Kanai, T., Hayashi, M., Kasai, T., Oshima, T., and Shiomi, D. (2021). Direct observation of
- conversion from walled cells to wall-deficient L-form and vice versa in Escherichia coli indicates the
- essentiality of the outer membrane for proliferation of L-form cells. Front. Microbiol. 12, 645965
- 766 Cho, H., Uehara, T., and Bernhardt, T. G. (2014). Beta-lactam antibiotics induce a lethal malfunctioning of 767 the bacterial cell wall synthesis machinery. *Cell* 159, 1300–1311
- 768 Cho, H., Wivagg, C. N., Kapoor, M., Barry, Z., Rohs, P. D. A., Suh, H., et al. (2016). Bacterial cell wall
- biogenesis is mediated by SEDS and PBP polymerase families functioning semi-autonomously. *Nat.*
- 770 *Microbiol.* 1, 16172
- 771 Chung, H. S., Yao, Z., Goehring, N. W., Kishony, R., Beckwith, J., and Kahne, D. (2009). Rapid β -lactam-
- induced lysis requires successful assembly of the cell division machinery. *Proc. Natl. Acad. Sci. USA*
- 773 106, 21872–21877
- 774 Chure, G., Lee, H. J., Rasmussen, A., and Phillips, R. (2018). Connecting the dots between
- mechanosensitive channel abundance, osmotic shock, and survival at single-cell resolution. *J. Bacteriol.*
- 776 200, e00460–18
- 777 Claessen, D. and Errington, J. (2019). Cell wall deficiency as a coping strategy for stress. *Trends Microbiol*.
- 778 27, 1025–1033
- 779 Curtis, N. A. C., Orr, D., Ross, G. W., and Boulton, M. G. (1979). Affinities of penicillins and
- 780 cephalosporins for the penicillin binding proteins of Escherichia coli k-12 and their antibacterial
- 781 activity. Antimicrob. Agents Chemother. 16, 533–539
- 782 Cushnie, T. P. T., O'Driscoll, N. H., and Lamb, A. J. (2016). Morphological and ultrastructural changes in
- bacterial cells as an indicator of antibacterial mechanism of action. Cell. Mol. Life Sci. 73, 4471–4492
- 784 Cussler, E. L. (1997). *Diffusion: Mass Transfer in Fluid Systems* (Cambridge University Press)
- 785 Daly, K. E., Huang, K. C., Wingreen, N. S., and Mukhopadhyay, R. (2011). Mechanics of membrane
- bulging during cell-wall disruption in Gram-negative bacteria. *Phys. Rev. E Stat. Nonlin. Soft Matter*
- 787 *Phys.* 83, 041922
- 788 Deng, Y., Sun, M., and Shaevitz, J. W. (2011). Direct measurement of cell wall stress stiffening and turgor
- pressure in live bacterial cells. *Phys. Rev. Lett.* 107, 158101
- 790 Dion, M. F., Kapoor, M., Sun, Y., Wilson, S., Ryan, J., Vigouroux, A., et al. (2019). Cell diameter in
- 791 Bacillus subtilis is determined by the opposing actions of two distinct cell wall synthetic systems. Nat.
- 792 *Microbiol.* 4, 1294–1305
- 793 Domínguez-Escobar, J., Chastanet, A., Crevenna, A. H., Fromion, V., Wedlich-Söldner, R., and Carballido-
- 794 López, R. (2011). Processive movement of MreB-associated cell wall biosynthetic complexes in bacteria.
- 795 Science 333, 225–228
- 796 Edwards, M. D., Black, S., Ramussen, T., Rasmussen, A., Stokes, N. R., Stephen, T.-L., et al. (2012).
- 797 Characterization of three novel mechanosensitive channel activities in *Escherichia coli*. *Channels* 6,
- 798 272-281
- 799 Emiola, A., George, J., and Andrews, S. S. (2015). A complete pathway model for lipid a biosynthesis in
- 800 Escherichia coli. PLoS ONE 10, e0121216
- 801 Erickson, H. P. (2017). How bacterial cell division might cheat turgor pressure a unified mechanism of
- septal division in gram-positive and gram-negative bacteria. *Bioessays* 39, 1700045
- 803 Erickson, H. P. (2021). How teichoic acids could support a periplasm in Gram-positive bacteria, and let
- cell division cheat turgor pressure. Front. Microbiol. 12, 664704

805 Falconer, S. B., Czarny, T. L., and Brown, E. D. (2011). Antibiotics as probes of biological complexity.

- 806 Nat. Chem. Biol. 7, 415–423
- Felle, H., Porter, J. S., Slayman, C. L., and Kaback, H. R. (1980). Quantitative measurements of membrane potential in *Escherichia coli*. *Biochemistry* 19, 3585–3590
- Furchtgott, L., Wingreen, N. S., and Huang, K. C. (2011). Mechanisms for maintaining cell shape in rod-shaped Gram-negative bacteria. *Mol. Microbiol.* 81, 340–353
- 811 Garner, E. C., Bernard, R., Wang, W., Zhuang, X., Rudner, D. Z., and Mitchison, T. (2011). Coupled,
- circumferential motions of the cell wall synthesis machinery and MreB filaments in *B. subtilis. Science* 333, 222–225
- Gitai, Z., Dye, N. A., Reisenauer, A., Wachi, M., and Shapiro, L. (2005). MreB actin-mediated segregation of a specific region of a bacterial chromosome. *Cell* 120, 329–341
- 816 Goodman, L. A. (1960). On the exact variance of products. J. Am. Stat. Assoc. 55, 708-713
- Gower, P. E. and Dash, C. H. (1969). Cephalexin: human studies of absorption and excretion of a new cephalosporin antibiotic. *Br. J. Pharmac.* 37, 738–747
- 819 Harbor, C. S. (2010). M9 minimal medium (standard). Cold Spring Harbor Protocols 2010
- Haswell, E. S., Phillips, R., and Rees, D. C. (2011). Mechanosensitive channels: what can they do and how do they do it? *Structure* 19, 1356–1369
- 822 Hegde, S. (2020). Dissertation: Escherichia coli's response to hypoosmotic shocks. Univ. Edinburgh
- Höltje, R. V. (1998). Growth of the stress-bearing and shape-maintaining murein sacculus of *Escherichia coli. Microbiol. Mol. Biol. Rev.* 62, 181–220
- 825 Huang, K. C., Mukhopadhyay, R., Wen, B., Gitai, Z., and Wingreen, N. S. (2008). Cell shape and
- cell-wall organization in Gram-negative bacteria. Proc. Natl. Acad. Sci. USA 105, 19282–19287.
- doi:10.1073/pnas.0805309105
- Hussain, S., Wivagg, C., Szwedziak, P., Wong, F., Schaefer, K., Izoré, T., et al. (2018). MreB filaments create rod shape by aligning along principal membrane curvature. *eLife* 7, e32471
- Hwang, H., Paracini, N., Parks, J. M., Lakey, J. H., and Gumbart, J. C. (2018). Distribution of mechanical stress in the *Escherichia coli* cell envelope. *Biochim. Biophys. Acta Biomembr.* 1860, 2566–2575
- Jones, L. J., Carballido-López, R., and Errington, J. (2001). Control of cell shape in bacteria: helical,
 actin-like filaments in *Bacillus subtilis*. *Cell* 104, 913–922
- Kocaoglu, O. and Carlson, E. E. (2015). Profiling of β -lactam selectivity for penicillin-binding proteins in *Escherichia coli* strain DC2. *Antimicrob. Agents Chemother.* 59, 2785–2790
- 836 Koch, A. L. (1983). The surface stress theory of microbial morphogenesis. *Adv. Microb. Physiol.* 24, 301–366
- Kohanski, M. A., Dwyer, D. J., and Collins, J. J. (2010). How antibiotics kill bacteria: from targets to networks. *Nat. Rev. Microbiol.* 8, 423–435
- Lan, G., Wolgemuth, C. W., and Sun, S. X. (2007). Z-ring force and cell shape during division in rod-like bacteria. *Proc. Natl. Acad. Sci. USA* 104, 16110–16115
- 842 Levina, N., Totemeyer, S., Stokes, N. R., Louis, P., Jones, M. A., and Booth, I. R. (1999). Protection
- of Escherichia coli cells against extreme turgor by activation of MscS and MscL mechanosensitive
- channels: identification of genes required for MscS activity. *EMBO J.* 18, 1730–1737
- 845 Lewis, K. (2010). Persister cells. *Annu. Rev. Microbiol.* 64, 357–372
- 846 Li, F., Chan, C. U., and Ohl, C. D. (2013). Yield strength of human erythrocyte membranes to impulsive
- 847 stretching. *Biophys. J.* 105, 872–879
- 848 Lo, C.-J., Leake, M. C., Pilizota, T., and Berry, R. M. (2007). Nonequivalence of membrane voltage and
- ion-gradient as driving forces for the bacterial flagellar motor at low load. *Biophys. J.* 93, 294–302

850 Meeske, A. J., Riley, E. P., Robins, W. P., Uehara, T., Mekalanos, J. J., Kahne, D., et al. (2016). SEDS

- proteins are a widespread family of bacterial cell wall polymerases. *Nature* 537, 634–638
- 852 Mickiewicz, K. M., Kawai, Y., Drage, L., Gomes, M. C., Davison, F., Pickard, R., et al. (2019). Possible
- role of L-form switching in recurrent urinary tract infection. *Nat. Commun.* 10, 4379
- 854 Milo, R. and Phillips, R. (2015). *Cell Biology by the Numbers* (Garland Science)
- 855 Movva, N. R., Nakamura, K., and Inouye, M. (1980). Regulatory region of the gene for the ompA protein,
- a major outer membrane protein of Escherichia coli. Proc. Natl. Acad. Sci. USA 77, 3845–3849
- Naismith, J. H. and Booth, I. R. (2012). Bacterial mechanosensitive channels—MscS: Evolution's solution
- 858 to creating sensitivity in function. *Annu. Rev. Biophys.* 41, 157–177
- 859 Osawa, M. and Erickson, H. P. (2019). L form bacteria growth in low-osmolality medium. *Microbiology*
- 860 165, 842–851
- 861 Paradis-Bleau, C., Markovski, M., Uehara, T., Lupoli, T. J., Walker, S., Kahne, D. E., et al. (2010).
- Lipoprotein cofactors located in the outer membrane activate bacterial cell wall polymerases. *Cell* 143,
- 863 1110-1120
- Peters, J. M., Colavin, A., Shi, H., Czarny, T. L., Larson, M. H., Wong, S., et al. (2016). A comprehensive,
- CRISPR-based approach to functional analysis of essential genes in bacteria. *Cell* 165, 1493–1506
- 866 Pilizota, T. and Shaevitz, J. W. (2012). Fast, multiphase volume adaptation to hyperosmotic shock by
- 867 Escherichia coli. PLoS ONE 7, e35205
- 868 Pilizota, T. and Shaevitz, J. W. (2014). Origins of *Escherichia coli* growth rate and cell shape changes at
- high external osmolality. Biophys. J. 107, 1962–1969
- 870 Qiao, Y., Srisuknimit, V., Rubino, F., Schaefer, K., Ruiz, N., Walker, S., et al. (2017). Lipid II
- overproduction allows direct assay of transpeptidase inhibition by β -lactams. *Nat. Chem. Biol.* 13,
- 872 793-798
- 873 Ramijan, K., Ultee, E., Willemse, J., Zhang, Z., Wondergem, J. A. J., van der Meij, A., et al. (2018).
- Stress-induced formation of cell wall-deficient cells in filamentous actinomycetes. *Nat. Commun.* 9,
- 875 5164
- 876 Ramos, S., Schuldiner, S., and Kaback, H. R. (1976). The electrochemical gradient of protons and its
- relationship to active transport in *Escherichia coli* membrane vesicles. *Proc. Natl. Acad. Sci. USA* 73,
- 878 1892–1896
- 879 Renner, L. D. (2019). Engineering bacterial shape using soft matter microchambers. Curr. Protoc. Chem.
- 880 *Biol.* 11, e59
- 881 Renner, L. D. and Weibel, D. B. (2011). Cardiolipin microdomains localize to negatively curved regions of
- 882 Escherichia coli membranes. Proc. Natl. Acad. Sci. USA 108, 6264–6269
- 883 Reuter, M., Hayward, N. J., Black, S. S., Miller, S., Dryden, D. T. F., and Booth, I. R. (2013).
- Mechanosensitive channels and bacterial cell wall integrity: does life end with a bang or a whimper? *J.*
- 885 *R. Soc. Interface* 11, 20130850
- 886 Rojas, E., Theriot, J. A., and Huang, K. C. (2014). Response of Escherichia coli growth rate to osmotic
- 887 shock. Proc. Natl. Acad. Sci. USA 111, 7807–7812
- 888 Rojas, E. R., Billings, G., Odermatt, P. D., Auer, G. K., Zhu, L., Miguel, A., et al. (2018). The outer
- membrane is an essential load-bearing element in Gram-negative bacteria. *Nature* 559, 617–621
- 890 Schumann, U., Edwards, M. D., Rasmussen, T., Bartlett, W., van West, P., and Booth, I. R. (2010). YbdG
- in Escherichia coli is a threshold-setting mechanosensitive channel with MscM activity. Proc. Natl.
- 892 Acad. Sci. USA 107, 12664–12669
- 893 Shaevitz, J. W. (2018). Microbiology: peeling back the layers of bacterial envelope mechanics. Curr. Biol.
- 894 28, R1210-R1211

895 Silhavy, T. J., Kahne, D., and Walker, S. (2010). The bacterial cell envelope. *Cold Spring Harb. Perspect*. 896 *Biol.* 2, a000414

- Sleator, R. D. and Hill, C. (2002). Bacterial osmoadaptation: the role of osmolytes in bacterial stress and virulence. *FEMS Microbiol. Rev.* 26, 49–71
- Sochacki, K. A., Shkel, I. A., Record, M. T., and Weisshaar, J. C. (2011). Protein diffusion in the periplasm of *e. coli* under osmotic stress. *Biophys J.*, 22–31
- 901 Sperelakis, N. (1995). *Cell Physiology Source Book: Essentials of Membrane Biophysics* (Academic 902 Press)
- 903 Sun, Y., Sun, T.-L., and Huang, H. W. (2014). Physical properties of *Escherichia coli* spheroplast membranes. *Biophys. J.* 107, 2082–2090
- Thévenaz, P., Ruttimann, U., and Unser, M. (1998). A pyramid approach to subpixel registration based on intensity. *IEEE Trans. Image Process.* 7, 27–41
- Thulin, E., Thulin, M., and Andersson, D. I. (2017). Reversion of high-level mecillinam resistance to susceptibility in *Escherichia coli* during growth in urine. *EBioMedicine* 23, 111–118
- Turner, R. D., Hurd, A. F., Cadby, A., Hobbs, J. K., and Foster, S. J. (2013). Cell wall elongation mode in Gram-negative bacteria is determined by peptidoglycan architecture. *Nat. Commun.* 4, 1496
- 911 Tuson, H. H., Auer, G. K., Renner, L. D., Hasebe, M., Tropini, C., Salick, M., et al. (2012). Measuring
- the stiffness of bacterial cells from growth rates in hydrogels of tunable elasticity. *Mol. Microbiol.* 85, 874–891
- Typas, A., Banzhaf, M., Gross, C. A., and Vollmer, W. (2012). From the regulation of peptidoglycan synthesis to bacterial growth and morphology. *Nat. Rev. Microbiol.* 10, 123–136
- 916 van Teeffelen, S. and Renner, L. D. (2018). Recent advances in understanding how rod-like bacteria stably 917 maintain their cell shapes. *F1000Res*. 7, 241
- 918 van Teeffelen, S., Wang, S., Furchtgott, L., Huang, K. C., Wingreen, N. S., Shaevitz, J. W., et al. (2011).
- The bacterial actin MreB rotates, and rotation depends on cell-wall assembly. *Proc. Natl. Acad. Sci. USA* 108, 15822–15827
- 921 Walsh, C. (2003). Antibiotics: Actions, Origins, Resistance (ASM Press)
- 922 Wang, S., Arellano-Santoyo, H., Combs, P. A., and Shaevitz, J. W. (2010). Actin-like cytoskeleton 923 filaments contribute to cell mechanics in bacteria. *Proc. Natl. Acad. Sci. USA* 107, 9182–9185
- Weibel, D. B., Diluzio, W. R., and Whitesides, G. M. (2007). Microfabrication meets microbiology. *Nat. Rev. Microbiol.* 5, 209–218
- 926 Wong, F. and Amir, A. (2019). Mechanics and dynamics of bacterial cell lysis. *Biophys. J.* 116, 2378–2389
- 927 Wong, F., Garner, E. C., and Amir, A. (2019). Mechanics and dynamics of translocating MreB filaments 928 on curved membranes. *eLife* 8, e40472
- 929 Wong, F., Renner, L. D., Özbaykal, G., Paulose, J., Weibel, D. B., van Teeffelen, S., et al. (2017).
- 930 Mechanical strain sensing implicated in cell shape recovery in *Escherichia coli*. *Nat. Microbiol*. 2, 931 17115
- 932 Wong, F., Stokes, J. M., Cervantes, B., Penkov, S., Friedrichs, J., Renner, L. D., et al. (2021). Cytoplasmic
- condensation induced by membrane damage is associated with antibiotic lethality. *Nat. Commun.* 12, 2321
- 935 Yao, Z., Kahne, D., and Kishony, R. (2012). Distinct single-cell morphological dynamics under beta-lactam antibiotics. *Mol. Cell* 48, 705–712
- 237 Zahir, T., Camacho, R., Vitale, R., Ruckebusch, C., Hofkens, J., Fauvart, M., et al. (2019). High-throughput
- time-resolved morphology screening in bacteria reveals phenotypic responses to antibiotics. *Commun.*
- 939 *Biol.* 2, 269

- 240 Zahir, T., Wilmaerts, D., Franke, S., Weytjens, B., Camacho, R., Marchal, K., et al. (2020). Image-based
- dynamic phenotyping reveals genetic determinants of filamentation-mediated β -lactam tolerance. *Front.*
- 942 *Microbiol.* 11, 00374
- 943 Zhao, H., Sun, Y., Peters, J. M., Gross, C. A., Garner, E. C., and Helmann, J. D. (2016). Depletion
- of undecaprenyl pyrophosphate phosphatases disrupts cell envelope biogenesis in *Bacillus subtilis*. *J*.
- 945 Bacteriol. 198, 2925–2935
- 946 Zheng, H., Ho, P.-Y., Jiang, M., Tang, B., Liu, W., Li, D., et al. (2016). Interrogating the Escherichia coli
- 947 cell cycle by cell dimension perturbations. *Proc. Natl. Acad. Sci. USA* 113, 15000–15005

11 FIGURES

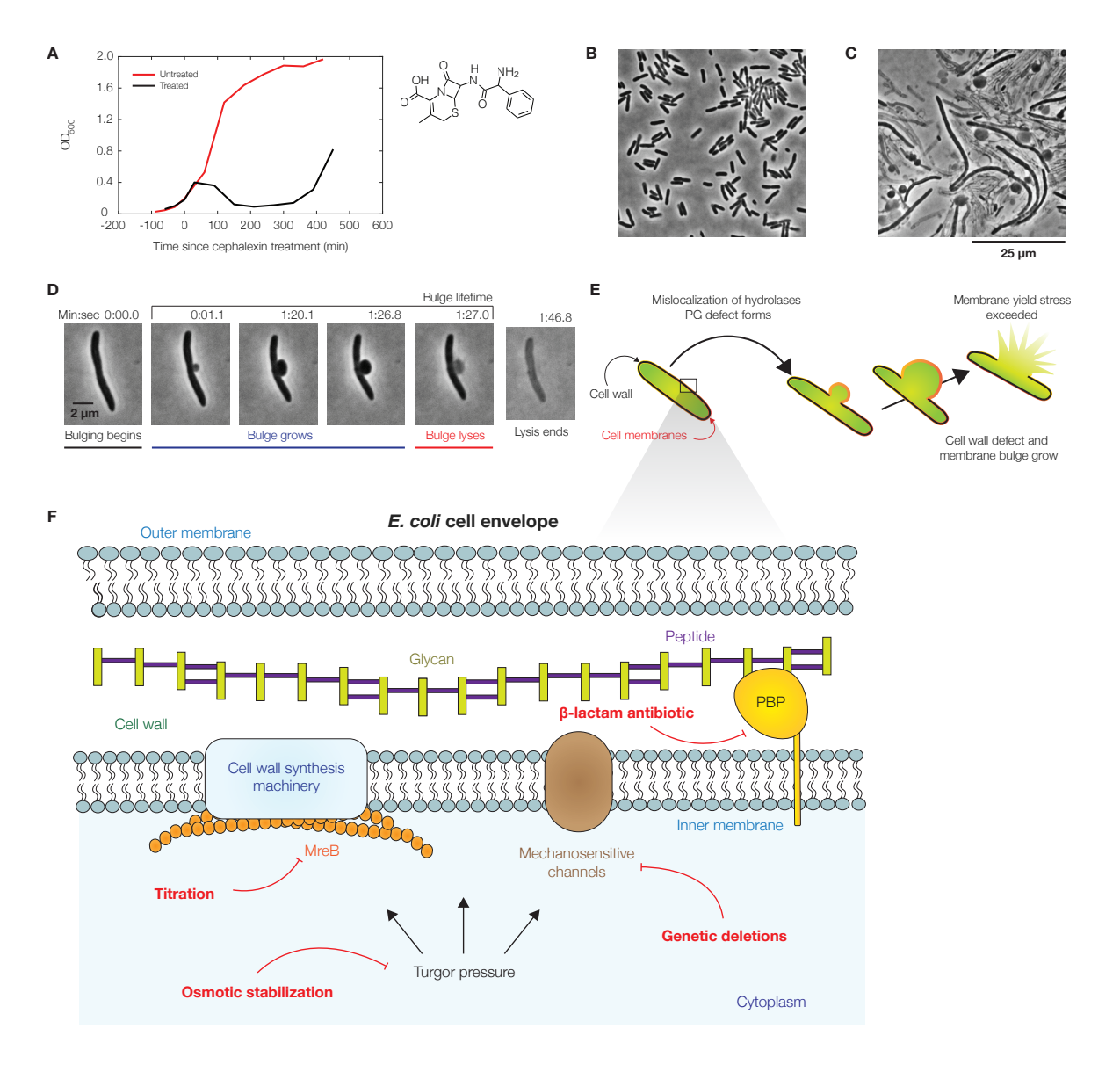


Figure 1. Dynamics of bacterial cell lysis.

- (A) Representative optical densities (OD₆₀₀) of a culture of wild-type *Escherichia coli* (strain MG1655) treated by cephalexin (50 μ g/mL), as shown at right. For comparison, measurements for an untreated culture are shown in red. Each curve shows one of two similar biological replicates.
- (B) Phase-contrast image of a population of *E. coli* cells immediately after cephalexin treatment. For a full timelapse, see Movie S1.
- (C) Phase-contrast image of the same population 2 h after cephalexin treatment, illustrating that membrane bulging and lysis are common within a population. For control experiments, see Figure S1.
- (D) Lysis dynamics of a representative log-phase *E. coli* cell during cephalexin treatment (50 μ g/mL), in which the cell membrane bulges and lyses. For a full timelapse, see Movie S2.
- (E) Schematic of a mechanical model which predicts the dynamics of membrane bulging and lysis. In this model, bulging arises due to membrane reorganization and the relaxation of the cell envelope, and swelling is caused by the continued growth of cell wall defects. Lysis occurs upon reaching a yield stress in the bulge. See *Methods* for details of the model.
- (F) Illustration of the *E. coli* cell envelope, with the perturbations considered in this work indicated in red.

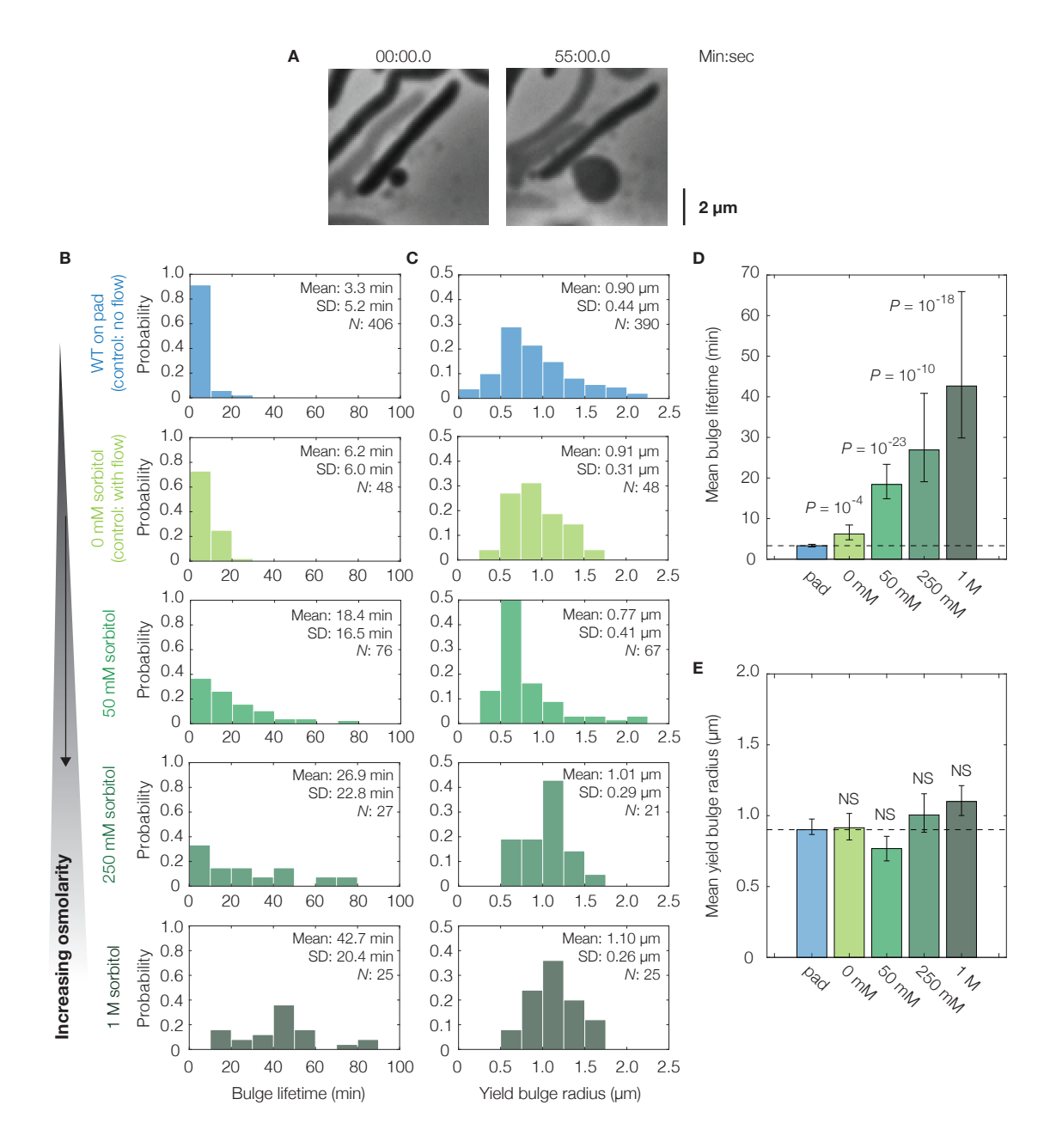


Figure 2. Osmotic delay of lysis in single cells.

(A) Representative bulging *E. coli* cell (strain MG1655) osmotically stabilized by flow of hyperosmotic media (250 mM sorbitol) after cephalexin (50 μ g/mL) treatment. For a full timelapse, see Movie S3; for model predictions in cells with reduced turgor, see Figure S2.

- (B) Distributions of bulge lifetimes for wild-type $E.\ coli$ cells either confined to LB-agarose pads containing cephalexin (WT, on pad) or under flow of LB containing cephalexin and sorbitol (sorbitol concentrations: 0 mM, 50 mM, 250 mM, and 1 M). Note that WT cells in 0 mM sorbitol differ from WT cells confined to pads in that an external flow was applied in the former. Here and below, the population mean, standard deviation (SD), and number of bulged cells (N) are indicated.
- (C) Same as (B), but for distributions of yield bulge radii.
- (D) Comparison of mean bulge lifetimes between control and osmotically shocked cells. Error bars indicate 95% confidence intervals, and p-values are indicated for two-sample Kolmogorov-Smirnov tests for the difference from wild-type (whose mean value is indicated by the dashed line).

(E) Same as (D), but for mean yield bulge radii. NS, not significant.

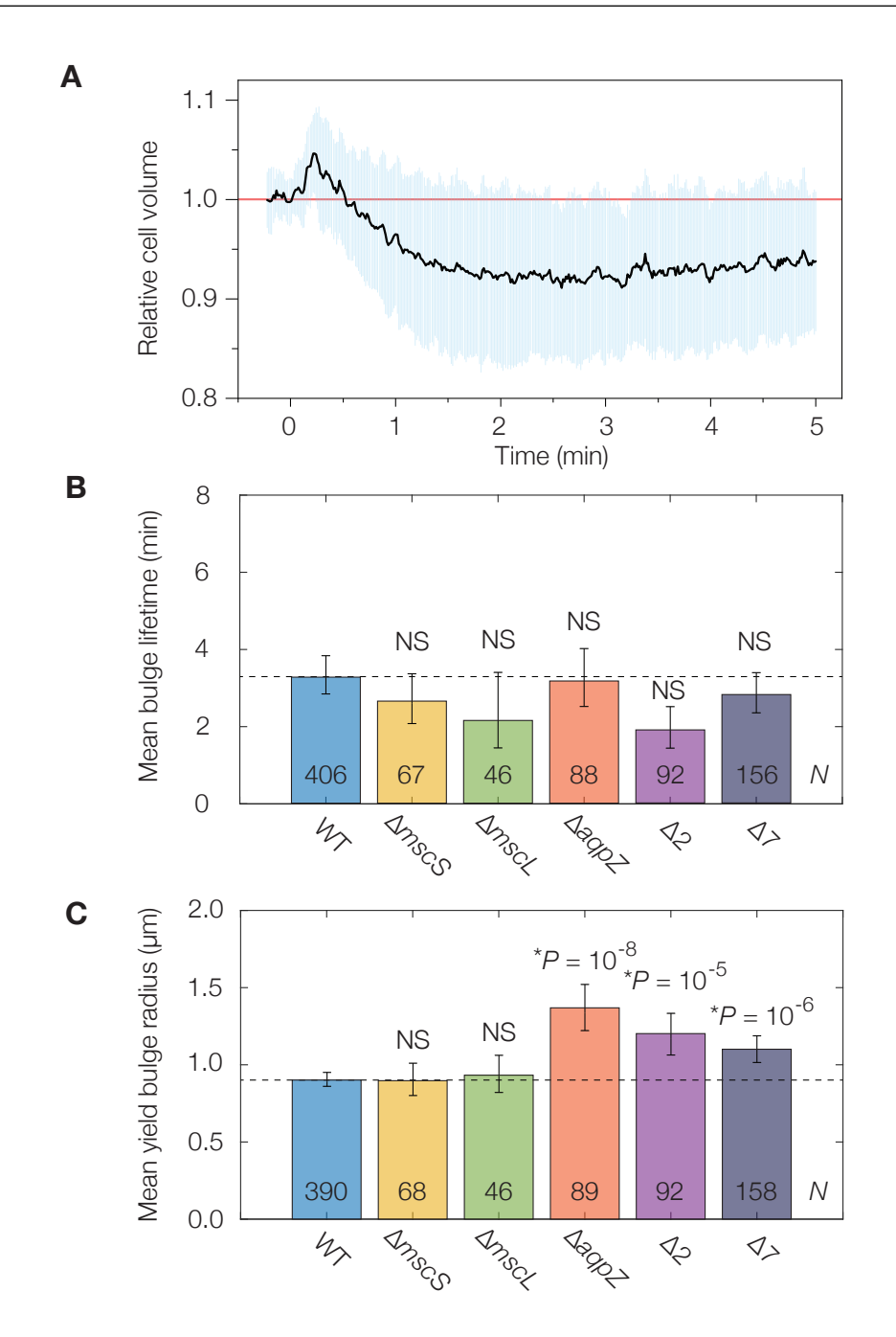


Figure 3. Mechanosensitive channels fail to delay or stabilize cells against lysis.

(A) Averaged single-cell volume response of 30 wild-type (parent strain BW25113) cells to a hypoosmotic shock of 600 mM sorbitol at time t=0 min, indicating volume recovery in \sim 30 s. Similar traces for the Δ 7 strain for an osmotic shock of a similar magnitude show no volume recovery, as detailed in Figure S7. The blue shaded region indicates one standard deviation.

(B) Comparison of mean bulge lifetimes between WT cells and MSC mutants. Error bars indicate 95% confidence intervals, and p-values are indicated for a two-sample Kolmogorov-Smirnov test for the difference from wild-type (dashed line). The number of bulged cells (N) is indicated on each bar. For detailed histograms, see Figure S7; for full timelapses of lysing populations, see Movies S4 and S5. NS, not significant.

(C) Same as (B), but for mean yield bulge radii. *While the yield bulge radii for the $\triangle aqpZ$, $\triangle 2$, and $\triangle 7$ strains differ from WT, we note they are not largely increased.

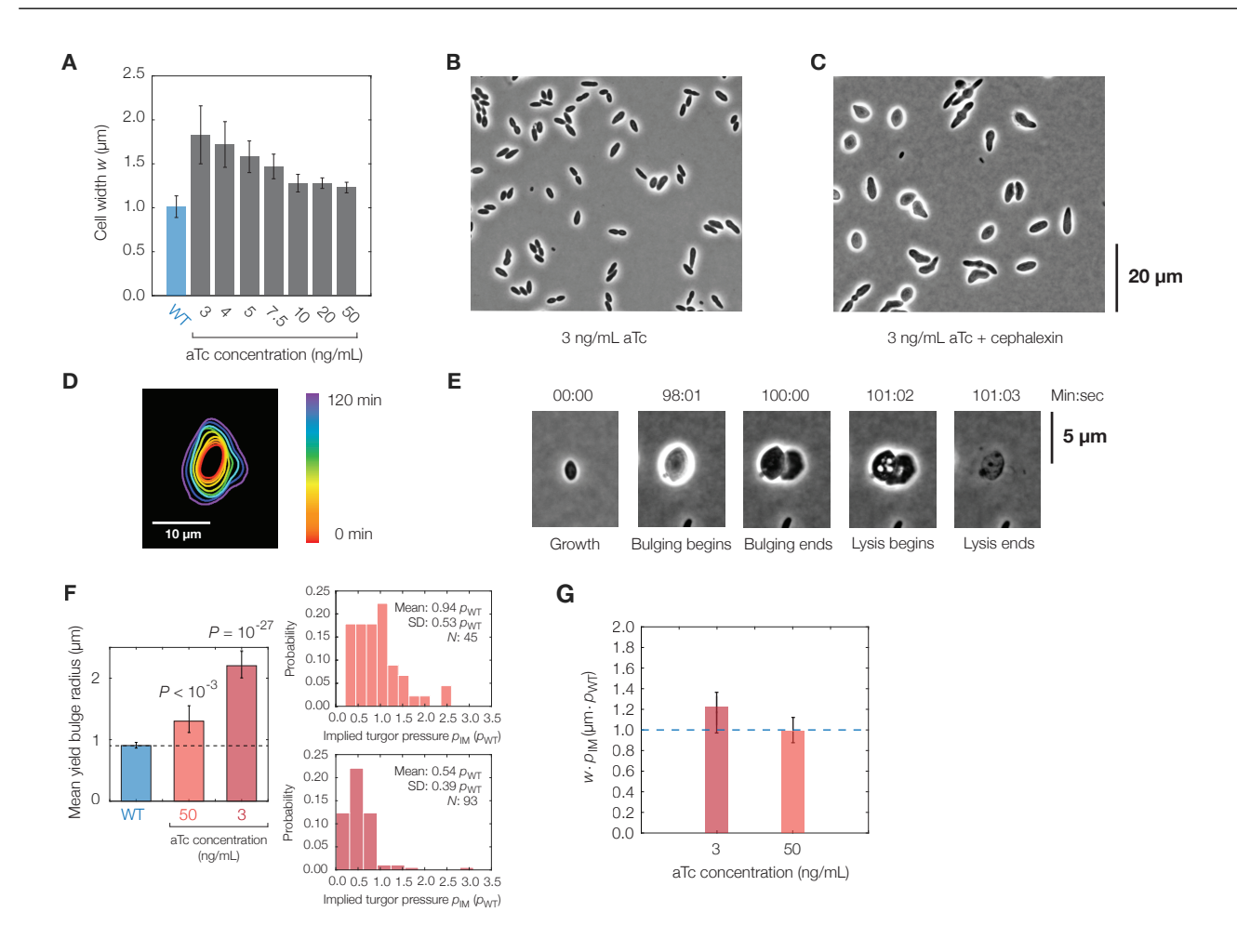


Figure 4. Effects of cell shape changes on lysis.

- (A) Plot of mean cell width against aTc concentration in the *mreB*-titratable strain (strain ZH1) and for wild-type (parent strain AMB1655) cells. Error bars indicate one standard deviation, and each bar represents at least 100 cells.
- (B) Phase-contrast image of a population of *mreB*-titratable cells, at an aTc concentration of 3 ng/mL, without cephalexin treatment.
- (C) Same as (B), but for 2 h after cephalexin treatment, showing that most cells lose their rod shapes.
- (D) Contour image of a representative *mreB*-titratable cell, at an aTc concentration of 3 ng/mL, which does not bulge or lyse over 2 h.
- (E) Lysis dynamics of a representative *mreB*-titratable cell, at an aTc concentration of 3 ng/mL, during cephalexin treatment, with labeling corresponding to Figure 1D. For a full timelapse of a lysing population, see Movie S6.
- (F) Comparison of mean yield bulge radii between WT and mreB-titratable cells. Error bars indicate 95% confidence intervals, and p-values refer to two-sample Kolmogolrov-Smirnov tests for the difference from wild-type (dashed line). The accompanying distributions of implied turgor pressures $p_{\rm IM}$, expressed in units of turgor pressure in wild-type cells, $p_{\rm WT}$, is shown at right. See Methods for details of the calculation.
- (G) Plot of the product of cell width, w, and implied turgor pressure, $p_{\rm IM}$, against aTc concentration in the mreB-titratable strain. Error bars represent 95% confidence intervals, and each point represents calculations based on measurements from at least 45 cells. The blue dashed line, shown for comparison, represents the value of $w \cdot p_{\rm IM}$ expected for a wild-type cell with a cell width of 1 μ m.



Supplementary Material

SUPPLEMENTARY MOVIES

Movie S1: Lysis dynamics of a population of *E. coli* cells. Movie S1 shows a representative population of wild-type *E. coli* (strain MG1655) cells in the time after cephalexin treatment. The time is indicated in hours:minutes: seconds, the time between frames is 1 min, and the timelapse covers a period of about 1.5 hrs. The field of view is approximately $126 \ \mu m \times 128 \ \mu m$.

Movie S2: Lysis dynamics of a representative *E. coli* cell. Movie S2 shows a representative wild-type *E. coli* (strain MG1655) cell in the time after cephalexin treatment. The time is indicated in minutes:seconds, the time between frames is 0.1 s, and the timelapse covers a period of about 15 mins. The field of view is approximately $16 \ \mu m \times 13 \ \mu m$.

Movie S3: Lysis dynamics of a representative, osmotically-stabilized *E. coli* cell. Movie S3 shows a representative wild-type *E. coli* (strain MG1655) cell in the time after cephalexin treatment, stabilized by flow of hyperosmotic media (250 mM sorbitol). The time is indicated in hours:minutes:seconds, the time between frames is 1 s, and the timelapse covers a period of about 1.25 hrs. The field of view is approximately $13 \ \mu m \times 13 \ \mu m$.

Movie S4: Lysis dynamics of a population of $\triangle aqpZ$ E. coli cells. Movie S4 shows a representative population of $\triangle aqpZ$ E. coli cells in the time after cephalexin treatment. The time is indicated in hours:minutes:seconds, the time between frames is 1 min, and the timelapse covers a period of about 1.5 hrs. The field of view is approximately $121 \ \mu m \times 129 \ \mu m$.

Movie S5: Lysis dynamics of a population of *E. coli* MSC mutants. Movie S5 shows a representative population of $\Delta 7$ *E. coli* cells in the time after cephalexin treatment. The time is indicated in minutes:seconds, the time between frames is 1 min, and the timelapse covers a period of about 45 mins. The field of view is approximately $127 \ \mu m \times 94 \ \mu m$.

Movie S6: Lysis dynamics of a population of *mreB*-titratable *E. coli* cells. Movie S6 shows a representative population of *mreB*-titratable *E. coli* cells in the time after cephalexin treatment, at a concentration of 3 ng/mL aTc. The time is indicated in hours:minutes:seconds, the time between frames is 1 min, and the timelapse covers a period of about 2 hrs. The field of view is approximately $128 \mu m \times 130 \mu m$.

SUPPLEMENTARY REFERENCES

- Amir, A., Babaeipour, F., McIntosh, D. B., Nelson, D. R., and Jun, S. (2014). Bending forces plastically deform growing bacterial cell walls. *Proc. Natl. Acad. Sci. USA* 111, 5778–5783
- Bialecka-Fornal, M., Lee, H. J., DeBerg, H. A., Gandhi, C. S., and Phillips, R. (2012). Single-cell census of mechanosensitive channels in living bacteria. *PLoS ONE* 7, 0033077
- Buda, R., Liu, Y., Yang, J., Hegde, S., Stevenson, K., Bai, F., et al. (2016). Dynamics of *Escherichia coli*'s passive response to a sudden decrease in external osmolarity. *Proc. Natl. Acad. Sci. USA* 113, E5838–E5846
- Cayley, D. S., Guttman, H. J., and Record, M. T. (2000). Biophysical characterization of changes in amounts and activity of *Escherichia coli* cell and compartment water and turgor pressure in response to osmotic stress. *Biophys. J.* 78, 1748–1764
- Çetiner, U., Rowe, I., Schams, A., Mayhew, C., Rubin, D., Anishkin, A., et al. (2017). Tension-activated channels in the mechanism of osmotic fitness in *Pseudomonas aeruginosa*. *J. Gen. Physiol.* 149, 595–609
- Chure, G., Lee, H. J., Rasmussen, A., and Phillips, R. (2018). Connecting the dots between mechanosensitive channel abundance, osmotic shock, and survival at single-cell resolution. *J. Bacteriol*. 200, e00460–18
- Deng, Y., Sun, M., and Shaevitz, J. W. (2011). Direct measurement of cell wall stress stiffening and turgor pressure in live bacterial cells. *Phys. Rev. Lett.* 107, 158101
- Hegde, S. (2020). Dissertation: Escherichia coli's response to hypoosmotic shocks. Univ. Edinburgh
- Lan, G., Wolgemuth, C. W., and Sun, S. X. (2007). Z-ring force and cell shape during division in rod-like bacteria. *Proc. Natl. Acad. Sci. USA* 104, 16110–16115
- Naismith, J. H. and Booth, I. R. (2012). Bacterial mechanosensitive channels—MscS: Evolution's solution to creating sensitivity in function. *Annu. Rev. Biophys.* 41, 157–177
- Phillips, R., Kondev, J., Garcia, H., and Theriot, J. (2012). *Physical Biology of the Cell* (Taylor and Francis)
- Sperelakis, N. (1995). *Cell Physiology Source Book: Essentials of Membrane Biophysics* (Academic Press)
- Sun, Y., Sun, T.-L., and Huang, H. W. (2014). Physical properties of *Escherichia coli* spheroplast membranes. *Biophys. J.* 107, 2082–2090
- Tuson, H. H., Auer, G. K., Renner, L. D., Hasebe, M., Tropini, C., Salick, M., et al. (2012). Measuring the stiffness of bacterial cells from growth rates in hydrogels of tunable elasticity. *Mol. Microbiol.* 85, 874–891
- Wong, F. and Amir, A. (2019). Mechanics and dynamics of bacterial cell lysis. *Biophys. J.* 116, 2378–2389
- Yao, X., Jericho, M., Pink, D., and Beveridge, T. (1999). Thickness and elasticity of Gram-negative murein sacculi measured by atomic force microscopy. *J. Bacteriol.* 181, 6865–6875
- Yao, Z., Kahne, D., and Kishony, R. (2012). Distinct single-cell morphological dynamics under beta-lactam antibiotics. *Mol. Cell* 48, 705–712
- Zheng, H., Ho, P.-Y., Jiang, M., Tang, B., Liu, W., Li, D., et al. (2016). Interrogating the *Escherichia coli* cell cycle by cell dimension perturbations. *Proc. Natl. Acad. Sci. USA* 113, 15000–15005

SUPPLEMENTARY FIGURES

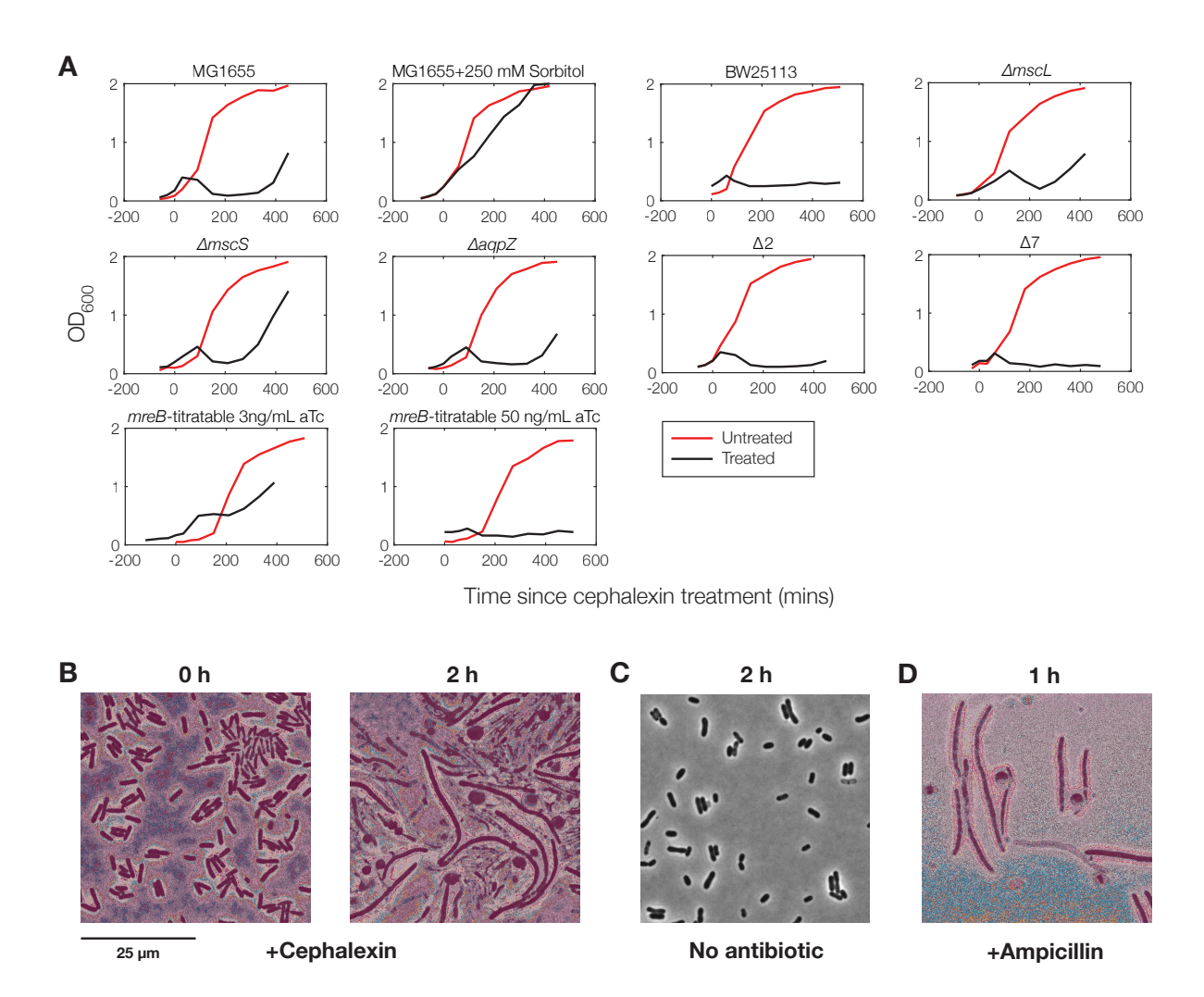


Figure S1. Experiments examining cell growth and responses to antibiotic treatment.

- (A) OD_{600} measurements of *E. coli* cultures untreated or treated by cephalexin across various strains and conditions. Each plot shows a different strain or condition considered in this study, and cephalexin (50 μ g/mL) was added to treated cultures in early-log phase, corresponding to an OD_{600} of approximately 0.2. Cells were grown in the conditions indicated before cephalexin treatment, so that the appropriate phenotypes were induced, with the exception of osmotic shocks, for which 250 mM sorbitol was added at the same time as cephalexin. Each curve is representative of two biological replicates.
- (B) Phase-contrast image of a population of *E. coli* (strain MG1655) cells immediately after cephalexin (50 μ g/mL) treatment (left), and phase-contrast image of the same population treated with cephalexin for 2 hrs (right), as shown in Figure 1B and 1C in the main text.
- (C) Phase-contrast image of a control population of *E. coli* cells corresponding to (B), but without cephalexin treatment, after 2 h.
- (D) Phase-contrast image of a population of E. coli cells treated with ampicillin (50 μ g/mL) for 1 hr.

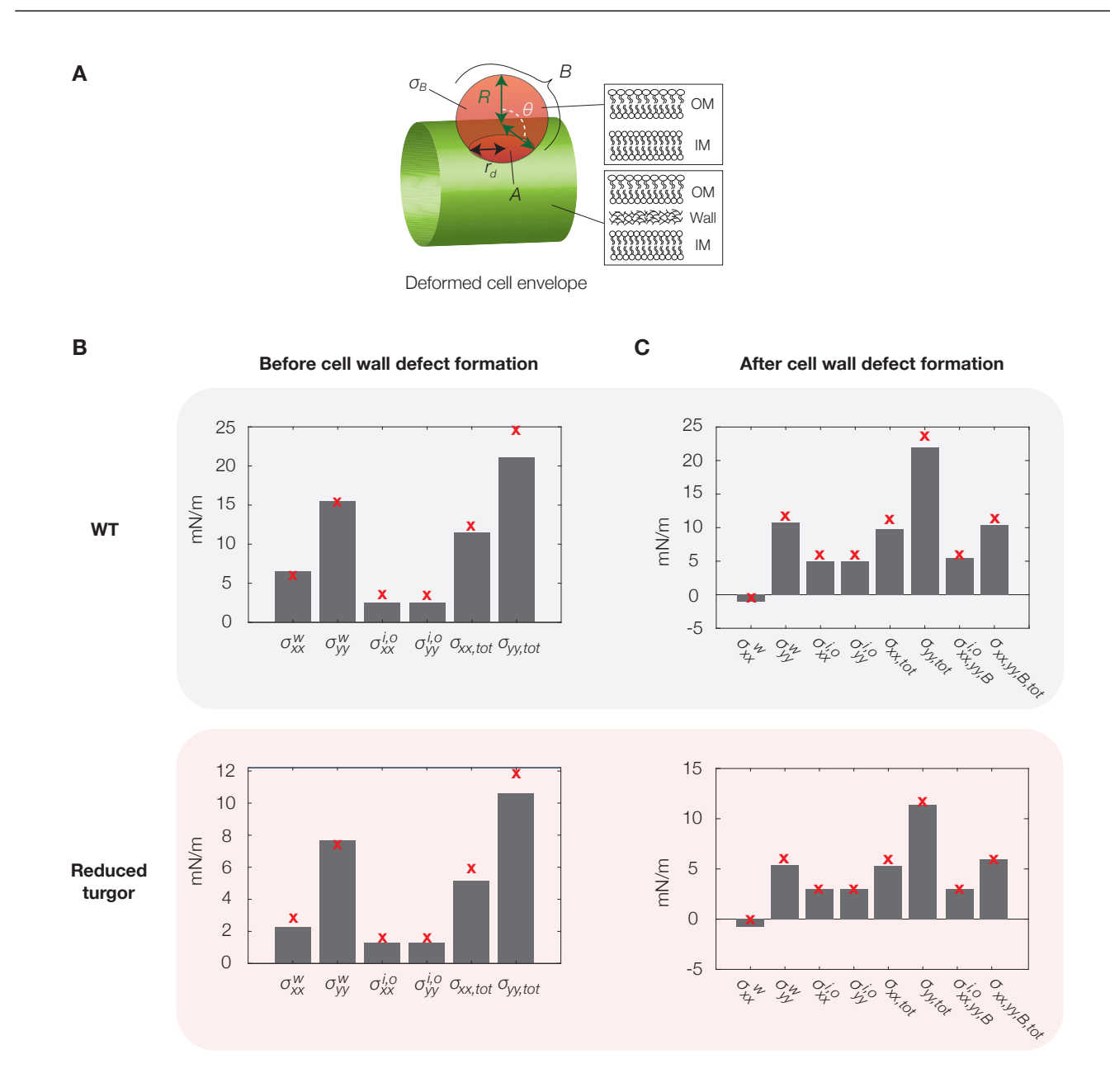


Figure S2. Model predictions for different perturbations considered in this work.

- (A) A schematic of the model, showing a bulged cell and its different variables. Here R denotes the radius of the bulge (indicated in the figure by B), θ the angle subtended by the bulge, r_d the radius of the cell wall defect (indicated in the figure by A), and σ_B the elastic stress in the bulge. IM and OM, inner membrane and outer membrane. The schematic is reproduced from (Wong and Amir, 2019).
- (B) Predicted cell envelope stress profiles before cell wall defect formation, for *E. coli* cells across varying conditions. The model parameters are summarized in Table S2. The '×' symbols indicate analytical predictions, while the bars indicate numerical results. "Reduced turgor" refers to the case where the number of solutes contained in the cell, corresponding to the turgor pressure, is halved. The subscript *tot* refers to the total stresses.
- (C) Same as (B), but after cell wall defect formation. In all cases, a constant cell wall defect radius of $r_d=0.5~\mu\mathrm{m}$ is assumed. The subscript B refers to stresses in the bulge.

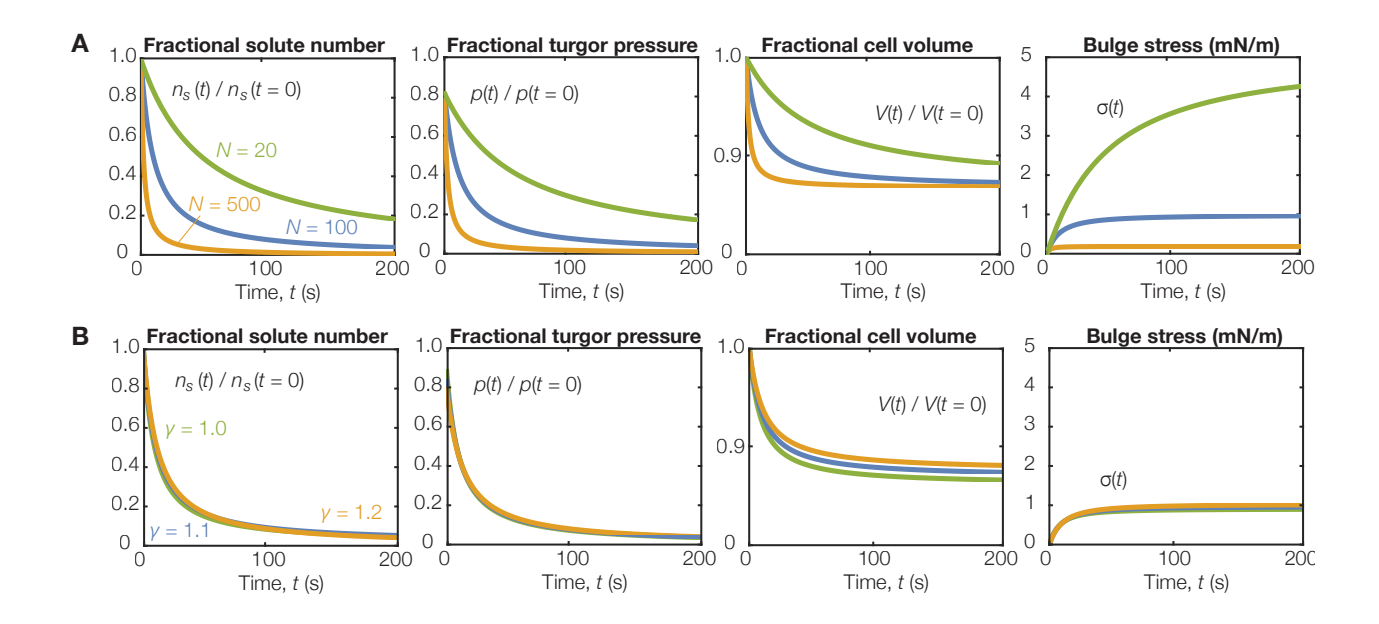


Figure S3. Transport model predictions for cellular variables after MSC gating. Plots of solute number, turgor pressure, cell volume, and bulge stress against time after MSC gating, for the parameter values summarized in Table S2. Model predictions describe the response of these variables to MSC gating and were determined by solving Eq. (17) in the *Methods*. Sensitivity analyses to (A) the number of gated MSCs, \mathcal{N} , with $\gamma=1.1$ and (B) the reference membrane area ratio, γ , with $\mathcal{N}=100$, are shown.

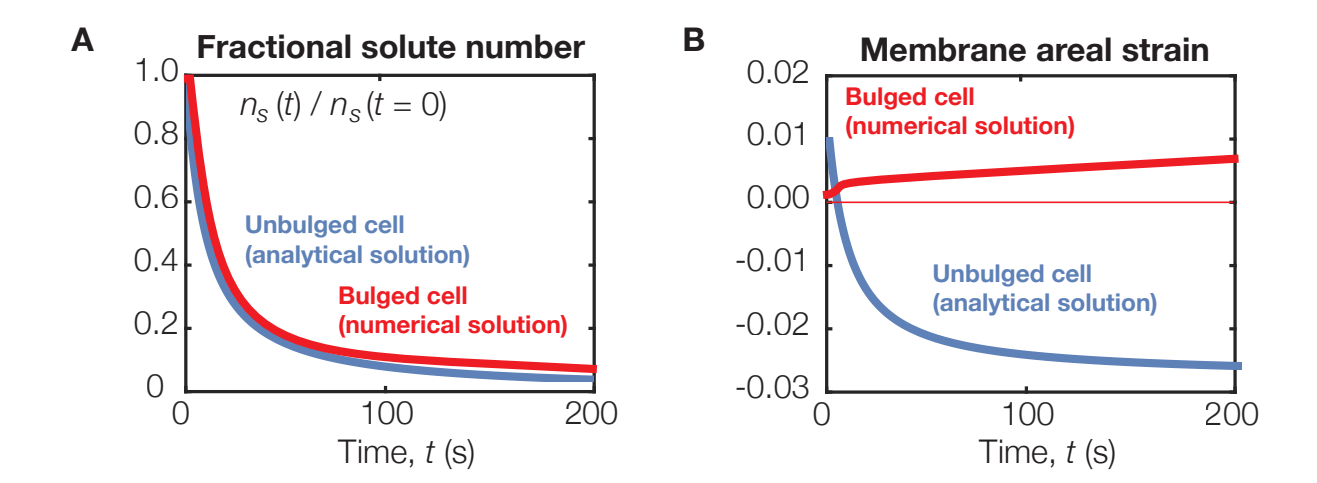


Figure S4. The bulged geometry does not change the predictions of solute outflow, but leads to increasing membrane stresses, in contrast to hypoosmotic shocks.

(A) Shown is a plot of the predicted solute number as a function of time, corresponding to Figure S3 and the parameter values for E. coli summarized in Table S2, with $\mathcal{N}=100$ and $\gamma=1.1$, for an unbulged cell (blue curve) as compared to a bulged cell (red curve). The numerical prediction for the unbulged cell is found by solving Eq. (17) in the Methods. The numerical prediction for the bulged cell is found by solving Eq. (9) in the Methods, assuming that the cell volume is determined by the bulging equation, Eq. (4) in the Methods.

(B) A plot of the bulge membrane strain as a function of time (red curve) and a plot of the membrane areal strain in a cylindrical cell without a bulge (blue curve). The numerical prediction for the bulge membrane strain is found by solving Eqs. (4) and (9) in the *Methods*. The numerical prediction for the membrane areal strain in a cylindrical cell is found by solving Eq. (17) in the *Methods*. In both cases, the parameters values used are summarized in Table S2, with $\mathcal{N}=100$ and $\gamma=1.1$. MSCs are assumed to be gated at t=0.

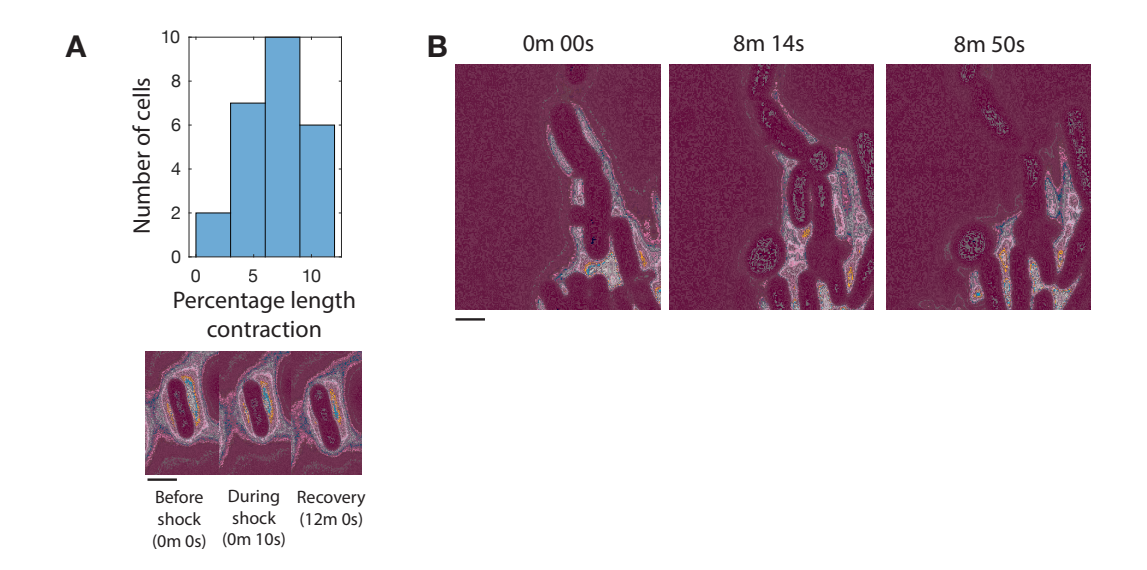


Figure S5. Control osmotic shock experiments and observation of membrane bulge detachment. (A) Hyperosmotic shock measurements in control, untreated $E.\ coli$ (strain MG1655) cells. The distribution of percentage changes in cell length after hyperosmotic shock by flow of growth media containing 500 mM sorbitol is shown for 25 cells. The inset shows a phase-contrast timelapse of one cell, with time indicated in minutes (m) and seconds (s). Scale bar, $1\ \mu m$.

(B) A sequence of timelapse images wherein a membrane bulge detaches from a bulged cell (strain MG1655) after flow of iso-osmotic media (drug-containing LB with 0 mM sorbitol). Scale bar, 1 μ m.

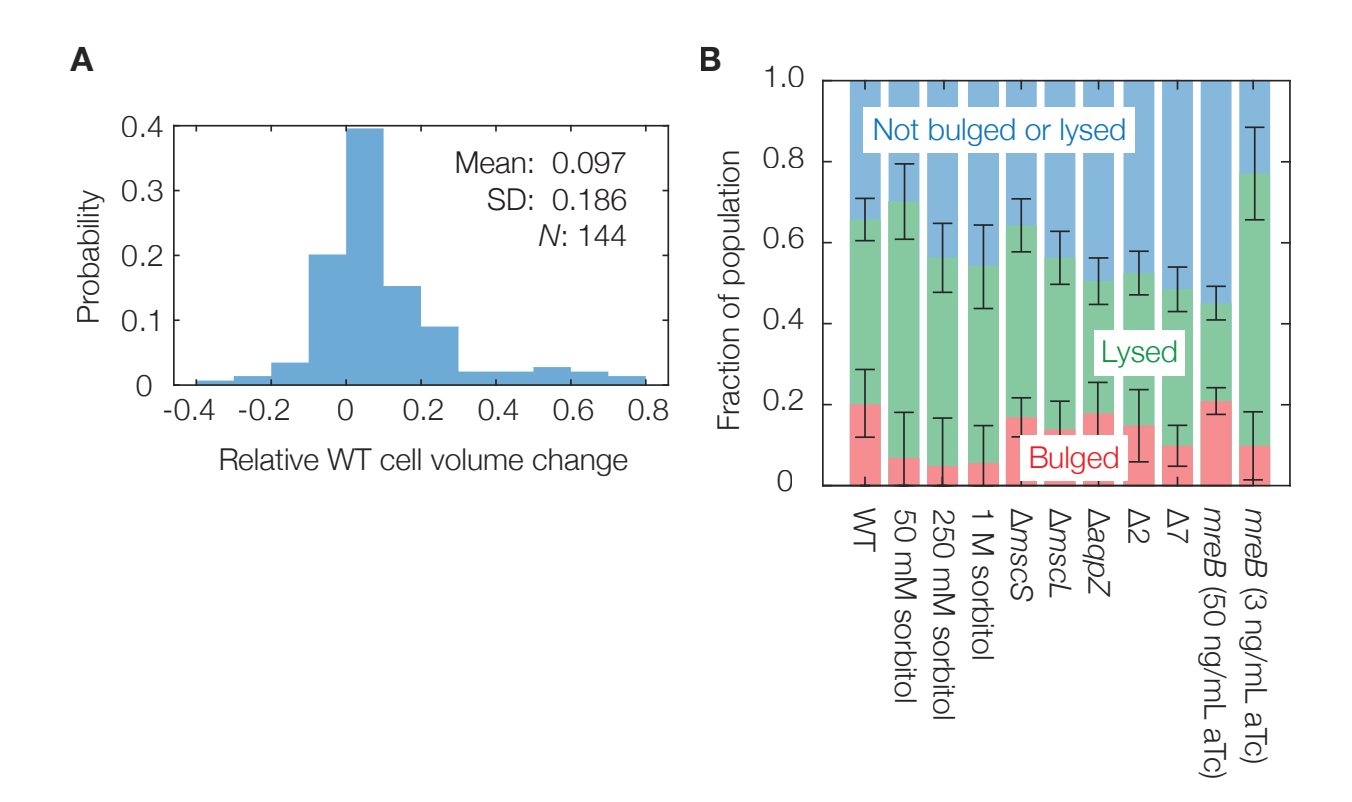


Figure S6. Cell size changes during bulging and bulging fractions in different strains and conditions.

(A) Distribution of relative cellular volume changes from before bulging to immediately before lysis in wild-type *E. coli* (strain MG1655) cells, showing that typical cellular volume changes are limited during bulging. *N* indicates number of bulged cells. Cellular dimensions were determined as discussed in *Methods*. (B) Fractions of bulged or lysed cells in different strains and conditions 2 hrs after cephalexin treatment, within each field of view comprising at least 50 cells. Data are representative of two to three biological replicates for each bar, and error bars indicate one standard deviation. *mreB*, *mreB*-titratable strain.

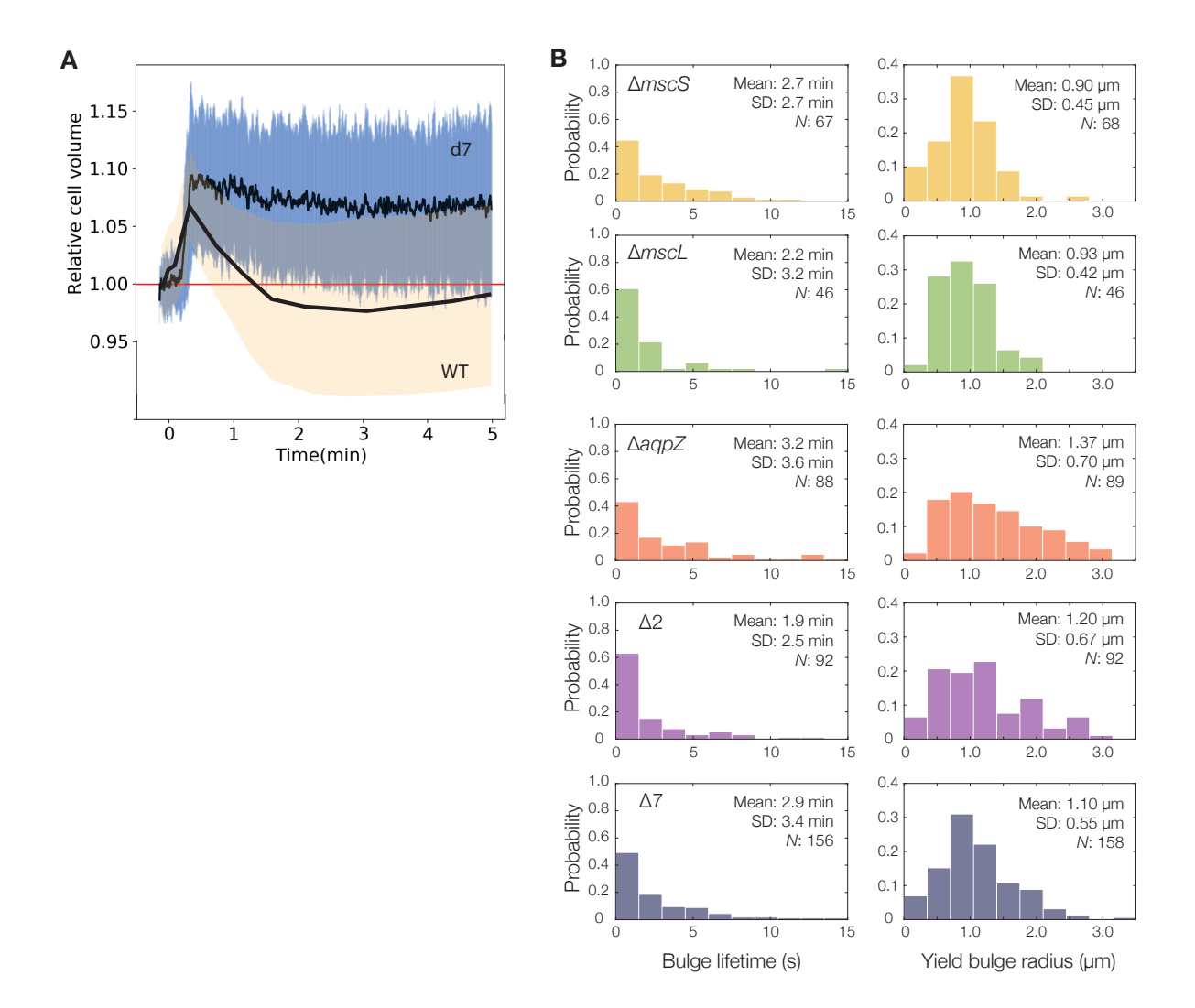


Figure S7. Characterization of MSC mutants.

(A) Average volume response for the relative cell volume of the $\Delta 7$ strain upon a 300 mM (460 mOsmol) hypoosmotic shock with NaCl in modified M9 media. The first 5 minutes following the hypoosmotic shock shows no volume recovery that is characteristic of MSC activation, as indicated by the sharp decrease in cellular volume after ~ 1 min in Figure 3A of the main text. The black curve shows the average response of individual single cell volumes (N=30), and the shaded region indicates one standard deviation. Images were captured every 0.33 s. Individual cell volume traces were first filtered with a median filter of window size 5 and aligned at the first point of maximum volume expansion. For comparison, measurements of the volume responses of wild-type cells (parent strain BW25113) in the same conditions, adapted from ref. (Buda et al., 2016), are shown.

(B) Distributions of bulge lifetimes and yield bulge radii for MSC mutants. For full timelapses of lysing populations, see Movies S4 and S5.

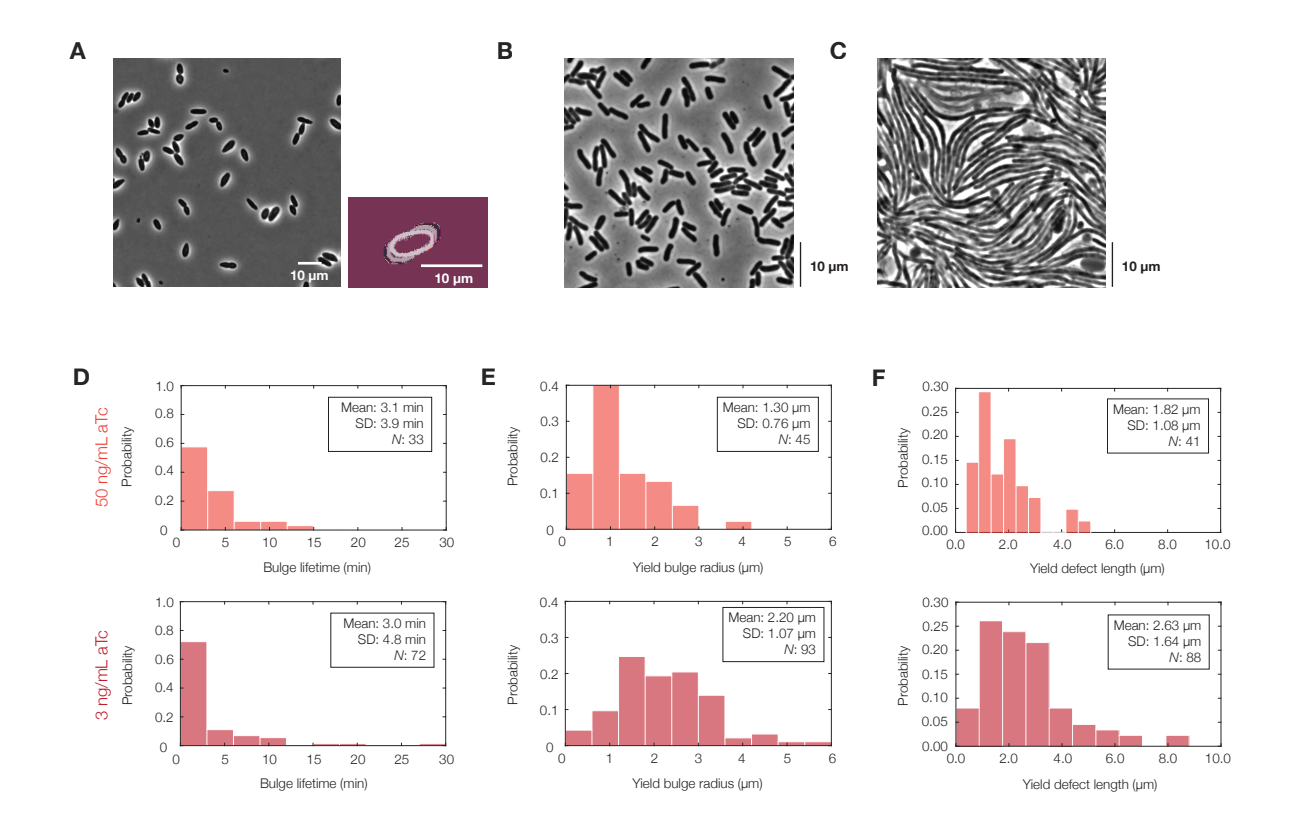


Figure S8. Additional measurements for mreB-titratable E. coli.

- (A) A population of control, untreated *mreB*-titratable cells 2 h after plating on an LB-agarose pad containing 3 ng/mL aTc. The *mreB*-titratable strain is described in previous work (Zheng et al., 2016). (Inset) A contour image corresponding to Figure 4D of the main text.
- (B) Phase-contrast image of a population of *mreB*-titratable cells, at an aTc concentration of 50 ng/mL, immediately after cephalexin (50 μ g/mL) treatment.
- (C) Same as (B), but 2 hrs after cephalexin (50 μ g/mL) treatment.
- (D-F) Distributions of bulge lifetimes (D), yield bulge radii (E), and yield defect lengths (F) for mreB-titratable cells at aTc concentrations of 3 and 50 ng/mL. The yield defect lengths r_d were estimated, according to the model, by the formula $R = r_d \sin \theta$, where R is the yield bulge radius and θ is the subtended angle of the bulge.

Strain	Genotype	Source	Cephalexin MIC
MG1655	F-, λ -, rph-1	Laboratory stock	20 μg/mL
JOE309	MC4100 araD+	Timelapse data from ref. (Yao et al., 2012)	20 μg/mL
BW25113	F-, Δ (araD-araB)567, Δ lacZ4787(::rrnB-3),	Gift from Thomas Bernhardt	20 μg/mL
	λ -, rph-1, Δ (rhaD-rhaB)568, hsdR514		
W3110	F-, λ-, IN(rrnD-rrnE)1, rph-1	Laboratory stock	20 μg/mL
JW2891-2 (Keio $\Delta mscS$)	BW25113 ΔmscS775::kan	Gift from Douglas Weibel	20 μg/mL
JW3252-1 (Keio $\Delta mscL$)	BW25113 ΔmscL727::kan	Gift from Douglas Weibel	20 μg/mL
JW0859-5 (Keio $\triangle aqpZ$)	BW25113 ∆aqpZ776::kan	Gift from Douglas Weibel	20 μg/mL
" $\Delta 2$ "	BW25113 ΔmscL727::kan,	Laboratory of Teuta Pilizota (Buda et al., 2016)	20 μg/mL
	∆mscS775::kan pWR21		
"Δ7"	20 μg/mL	Laboratory of Teuta Pilizota (Hegde, 2020)	20 μg/mL
AMB1655	F-, λ -, Δ fnr-267, rph-1; G>T gudD2917303, flhDC::IS	Antoine Danchin	Not determined
ZH1	AMB1655 mreB<>aph,	Laboratory of Chenli Liu (Zheng et al., 2016)	20 μg/mL (3-50 ng/mL aTc);
("mreB-titratable")	bla:Ptet-tetR-mreB at attB site		20-40 μg/mL (0 ng/mL aTc)

Table S1. Strains used in this study and their cephalexin MICs.

Variable	Value	Reference
Mechanical model of bacterial cell lysis		
Cell wall 2D elastic modulus (axial), $Y_r^w (= Y^w)$	0.1 N/m	(Deng et al., 2011; Amir et al., 2014; Tuson et al., 2012)
Cell wall 2D elastic modulus (circumferential), $Y_y^w (= Y^w)$	0.2 N/m	(Deng et al., 2011; Lan et al., 2007)
Inner membrane area-stretch modulus, $K_a^i (=K)$	0.1 N/m	(Sun et al., 2014)
Outer membrane area-stretch modulus, $K_a^o (= K)$	0.1 N/m	(Sun et al., 2014)
Cell wall Poisson's ratio, $\nu_{xy}^w (= \nu^w)$	0.2	(Yao et al., 1999)
Cell wall Poisson's ratio, $v_{ux}^{w} (= v^w)$	0.4	$ \nu_{yx}^{w} = Y_{y}^{w} \nu_{xy}^{w} / Y_{x}^{w} $ (Deng et al., 2011; Cayley et al., 2000)
Turgor pressure, p	0.5 atm	
Number of solute molecules inside a cell, n_s	9.5×10^{7}	$n_s \approx p[\pi(r_0^w)^2 L_0^w]/kT$
Reference cell wall radius, r_0^w	$0.5 \mu m$	This work
Reference cell wall length, \tilde{L}_0^w	$10 \mu\mathrm{m}$	This work
Reference membrane surface area ratio, γ	1.1	Intermediate value of the range inferred in (Wong and Amir, 2019)
Cell wall defect radius, r_d	$0.5 \mu m$	This work
Temperature, T	300 K	This work
Transport model of solute outflow		
Viscosity of water, μ	$8.9 \times 10^{-4} \mathrm{Pa} \cdot \mathrm{s}$	_
Density of water, ρ	997 kg/m^3	_
Volume occupied per water molecule, m_w	$3 \times 10^{-29} \text{ m}^3$	_
Characteristic MSC hole radius, r_c	1.5 nm	(Naismith and Booth, 2012; Buda et al., 2016)
Characteristic transport length across bilayer, L_c	10 nm	This work; membrane thickness estimate from (Phillips et al., 2012)
Characteristic number of gated channels, \mathcal{N}	100	(Bialecka-Fornal et al., 2012; Chure et al., 2018)
Membrane hydraulic conductivity, L_p	$10^{-12} \text{m}^3 / \text{N} \cdot \text{s}$	(Sperelakis, 1995; Çetiner et al., 2017)

Table S2. Model parameters for E. coli used in this study. Parameter value simplifications are indicated in parentheses.

				Exponential		Bootstrapped CI's	
	Condition	N	Mean	χ^2 test	<i>p</i> -value	LCI	UCI
Bulge lifetime (s)	WT	406	199.35	1	5.2E-11	173.07	233.45
_	WT+0 mM sorbitol	48	373.12	1	7.6E-03	280.67	482.94
	WT+50 mM sorbitol	76	1105.1	0	4.6E-01	909.42	1365.1
	WT+250 mM sorbitol	27	1615.2	0	N/A	1159.1	2165.7
	WT+1 M sorbitol	25	2559.5	0	N/A	1791.9	3955.1
	$\Delta mscS$	67	161.31	0	4.0E-01	126.25	204.92
	$\Delta mscL$	46	130.76	0	1.2E-01	87.69	207.2
	$\Delta aqpZ$	88	193.14	0	2.6E-01	153.23	244.81
	$\Delta 2$	92	115.39	0	1.6E-02	88.16	151.77
	$\Delta 7$	156	171.25	0	9.3E-02	142.81	206.32
	<i>mreB</i> -titratable (50 ng/mL aTc)	33	186.11	0	1.5E-02	120.78	279.98
	<i>mreB</i> -titratable (3 ng/mL aTc)	72	178.45	0	2.5E-02	125.59	267.92
				Logi	normal		
Yield bulge radius (μ m)	WT	390	0.9	1	1.8E-04	0.86	0.95
	WT+0 mM sorbitol	48	0.91	0	2.3E-01	0.83	1.01
	WT+50 mM sorbitol	67	0.77	1	9.6E-03	0.69	0.88
	WT+250 mM sorbitol	21	1.01	0	N/A	0.89	1.12
	WT+1 M sorbitol	25	1.10	0	N/A	1.00	1.21
	$\Delta mscS$	68	0.9	0	1.0E-01	0.8	1.01
	$\Delta mscL$	46	0.93	0	4.1E-02	0.82	1.06
	$\Delta aqpZ$	89	1.37	0	4.8E-01	1.22	1.52
	$\Delta 2$	92	1.2	0	2.5E-02	1.07	1.34
	Δ 7	158	1.1	1	1.1E-03	1.02	1.19
	mreB-titratable (50 ng/mL aTc)	45	1.3	0	1.2E-01	1.11	1.55
	<i>mreB</i> -titratable (3 ng/mL aTc)	93	2.2	0	5.6E-02	2	2.44

Table S3. Statistical testing of inferred distributions and calculated confidence intervals. Here N indicates sample size (numbers of bulged cells), LCI and UCI denotes the lower and upper bounds for the 95% confidence interval (CI) for the mean, respectively, and the test used is the χ^2 goodness-of-fit, where 1 indicates rejection of the null hypothesis that the data come from the distributions shown and 0 otherwise. N/A indicates that there are insufficient degrees-of-freedom for this test. The bootstrapped confidence intervals are calculated as detailed in *Methods*.